Fluid Phase Equilibria 575 (2023) 113913

Contents lists available at ScienceDirect

Fluid Phase Equilibria

journal homepage: www.sciencedirect.com/journal/fluid-phase-equilibria

Densities, viscosities, and diffusivities of loaded and unloaded aqueous CO_2/H_2S/MDEA mixtures: A molecular dynamics simulation study

H. Mert Polat [a], Casper van der Geest [a], Frédérick de Meyer [b,c], Céline Houriez [c], Thijs J.H. Vlugt [a], Othonas A. Moultos [a,*]

[a] Engineering Thermodynamics, Process & Energy Department, Faculty of Mechanical Engineering, Delft University of Technology, Leeghwaterstraat 39, Delft 2628CB, The Netherlands

[b] CO_2 and Sustainability R&D Program, Gas & Low Carbon Entity, OneTech, Total Energies S.E., 92078 Paris, France

[c] Mines Paris, PSL University, Center for Thermodynamics of Processes (CTP), 77300 Fontainebleau, France

ARTICLE INFO

Keywords:
Molecular dynamics
Carbon dioxide
Hydrogen sulfide
Transport properties
Diffusion
MDEA

ABSTRACT

Experimentally measuring the diffusivities of CO_2 and H_2S in aqueous alkanolamine solutions presents an extremely challenging task. To overcome this challenge, we performed Molecular Dynamics (MD) simulations to study the effects of temperature and *N*-methyldiethanolamine (MDEA) concentration on self-diffusivities of CO_2 (D_{CO_2}) and H_2S (D_{H_2S}) in aqueous MDEA solutions. We compute the densities and viscosities of aqueous MDEA solutions for an MDEA concentration range of 10–50 wt% and a temperature range of 288–333 K showing an excellent agreement with experimental data from literature. We compute the self-diffusivity of MDEA (D_{MDEA}) in aqueous MDEA solutions and our findings show that the computed values of D_{MDEA} are in excellent agreement with experimental and simulation results from literature. The self-diffusivities D_{CO_2} and D_{H_2S} in aqueous MDEA solutions are computed for a wide range of temperatures and MDEA concentrations and our results show that both D_{CO_2} and D_{H_2S} depend significantly on temperature and MDEA concentration. We also show that both CO_2 and H_2S diffuse slower in aqueous MDEA solutions than in aqueous MEA solutions. By comparing the radial distribution functions of CO_2, H_2S, water, and MDEA, we show that H_2S has stronger interactions with the surrounding molecules than CO_2, which makes H_2S diffuse slower in aqueous MDEA solutions. We also investigate the densities and viscosities of acid gas loaded aqueous MDEA solutions and self-diffusivities of the reaction products of CO_2 and H_2S with aqueous MDEA solutions. We show that the self-diffusivities of CO_2-loaded solutions significantly decrease with increasing CO_2 loading while the self-diffusivities of H_2S-loaded solutions do not change with changing H_2S loading. Our results will be helpful in the design and optimization of acid gas removal units.

1. Introduction

Natural gas combustion produces much lower particulate matter emissions and has the highest energy output per CO_2 emitted compared to other fossil fuels [1–3]. Therefore, natural gas has the potential to be a transition fuel that will decrease CO_2 emissions until large scale usage of renewable energy sources becomes feasible [4–6]. Using steam methane reforming [7–9], natural gas can also be used to produce hydrogen, an energy carrier with high gravimetric energy density and near-zero greenhouse gas emissions [10]. Unfortunately, 40% of the known natural gas sources have high concentrations of acid gases, specifically, more than 2 mol % of CO_2 and 100 ppm of H_2S [11]. Some reservoirs of natural gas in Southeast Asia and Australia can even have CO_2 concentrations of up to 80% [12]. CO_2 and H_2S can cause corrosion of the pipelines [13,14], and therefore, these components must be removed from the natural gas streams. Also, for safety reasons, H_2S must be removed since it is a toxic gas [15]. For transportation in pipelines, CO_2 and H_2S concentrations should be lower than 2 mol % and 4 ppm [16], respectively. In liquefied natural gas (LNG), CO_2 concentrations should be lower than 50 ppm [12] to eliminate the blockages caused by solid CO_2 in the liquefaction process. To this end, several different processes can be used to remove acid gases from natural gas streams such as membrane-based separation [17,18], cryogenic distillation [19,20], direct conversion of H_2S to elemental sulfur [21,22], adsorption-based separation [23–25], and absorption-based separation [11].

Absorption-based separation is commonly preferred as it is a mature and reliable process which also results in very low amounts of

* Corresponding author.
E-mail address: o.moultos@tudelft.nl (O.A. Moultos).

https://doi.org/10.1016/j.fluid.2023.113913
Received 17 June 2023; Received in revised form 22 July 2023; Accepted 31 July 2023
Available online 4 August 2023

absorbed (lost) methane [26–28]. This process uses liquid solvents to remove CO_2 and H_2S from natural gas streams [11,27,29,30], usually aqueous alkanolamine solvents which can absorb acid gases by physical and/or chemical absorption [11,26]. In absorption-based separation of acid gases, the natural gas stream flows through a high pressure column (usually at pressures of 20–100 bar [31]) at temperatures in the range of 313–353 K [32]. The acid gases come in contact with the solvent and are absorbed into the liquid phase. Another advantage of the absorption-based separation process is that the liquid solvents can be regenerated at high temperature (typically at 363–383 K) and reused. To optimize this process, process simulation software is typically used [33–36] which requires parameters such as the diffusion coefficients of the acid gases, and the viscosity and the density of the solvent [37]. Therefore, accurate knowledge of these properties is crucial for the process design of both the absorption and regeneration stages. Since CO_2 and H_2S react with the solvent, it is extremely challenging to experimentally measure their diffusivities in aqueous alkanolamine solvents. For this reason, estimates of the diffusion coefficients of acid gases are obtained by performing experiments with surrogate non-reacting molecules such as N_2O instead of CO_2 [38–40]. For example, Sada et al. [41] estimated the diffusion coefficient of CO_2 in aqueous solutions of different alkanolamines by measuring the diffusion coefficient of N_2O in these solutions. For more examples of the CO_2/N_2O analogy, the reader is referred to Refs. [38,42,43].

Molecular dynamics (MD) simulations with classical force fields are widely used to compute thermodynamic and transport properties (e.g., viscosities, densities, diffusion coefficients, phase equilibria) of aqueous solutions [2,44–54]. The main advantage of MD simulations for computing the diffusion coefficients of acid gases in aqueous alkanolamine solutions is that the reactions in the liquid phase are not considered, therefore, there is no need for surrogate non-reacting molecules in these simulations. Also, experiments can be expensive, time consuming, and dangerous at high pressures and temperatures. Despite the importance of thermodynamic and transport properties of these systems, literature data on the diffusion coefficients of CO_2 and H_2S, and their temperature and alkanolamine concentration dependency, are scarce. To validate the CO_2/N_2O analogy, Chen et al. [39] computed the diffusion coefficients of CO_2 and N_2O in aqueous monoethanolamine (MEA) solutions at 303 K. Melnikov et al. [55] computed the diffusion coefficients of CO_2 in aqueous MEA solutions for different loadings of CO_2 at 313 K. Yiannourakou et al. [11] computed the diffusion coefficients of *N*-methyldiethanolamine (MDEA) and CO_2 in 30 wt% MDEA/water solutions for a temperature range of 300–400 K. Recently, we computed viscosities of aqueous MEA solutions and self-diffusion coefficients of CO_2 and H_2S in 10–50 wt% MEA/water solutions at 293–353 K [2]. In line with experimental data, we showed that the MEA concentration in the solution significantly affects the self-diffusion coefficients of both CO_2 and H_2S [2].

Here, the self-diffusion coefficients of CO_2 and H_2S in aqueous MDEA solutions are computed for a wide range of temperatures and MDEA concentrations. We focus on MDEA solutions because it is a commonly used alkanolamine for selective acid gas removal from natural gas and biogas streams [56]. To validate the accuracy of the interaction potentials for the aqueous solutions of acid gases, we first computed self-diffusion coefficients of CO_2 and H_2S in pure water. Next, we computed the densities of aqueous MDEA solutions for a temperature range of 288–333 K and an MDEA concentration range of 10–50 wt% MDEA and compared our results with experimental data from literature. By introducing a scaling factor of 0.9 to the point charges of MDEA, we show that we can accurately compute the density of aqueous MDEA solutions. To validate the force field selection for MDEA, we compute viscosities of aqueous MDEA solutions for a temperature range of 288–333 K and an MDEA concentration range of 10–50 wt% MDEA, and compare the computed viscosities with experimental data from literature. We further validate the force field for MDEA by computing the self-diffusion coefficient of MDEA and comparing it with available data from literature. Next, the self-diffusion coefficients of CO_2 and H_2S in aqueous MDEA solutions are computed for a temperature range of 288–333 K and an MDEA concentration range of 10–50 wt% MDEA. Using radial distribution functions of the acid gases, water, and MDEA, we investigated the structural changes in the solutions as a function of MDEA concentration. Finally, we investigated the diffusivities of the acid gases and the reaction products from acid gas absorption in aqueous MDEA solutions (bicarbonate (HCO_3^-), bisulfide (CO_3^{2-}), and protonated MDEA ($MDEAH^+$) ions) as a function of acid gas loading in 50 wt% MDEA/water solutions at 313 K. The accurate knowledge of the self-diffusivities of the reaction products in acid gas loaded aqueous MDEA solutions is important since this shows how the mass transfer of these species change with changing acid gas loading [57–60].

Our results will be helpful in the optimization of an acid gas removal unit of a plant treating natural gas and biogas, and we anticipate that our study will motivate further research in computing transport properties of acid gases and the reaction products from acid gas absorption in aqueous alkanolamine solutions.

This article is organized as follows: the simulation methods and force fields are explained in Section 2. We discuss the results from our simulations and the comparison with available data from literature in Section 3. Our main findings are summarized in Section 4.

2. Simulation methods

All MD simulations in this study are performed using LAMMPS (version 2 June 2022) [61] on the DelftBlue supercomputer [62]. The widely used TIP4P/2005 classical force field [63] is used to model water. For CO_2 and H_2S, we use the TraPPE force field [64,65]. For the interactions between water and CO_2, we used the cross-interaction parameters optimized by Orozco et al. [66]. In our simulations, water, CO_2, and H_2S are considered nearly-rigid by using strong bond-stretching and bond-bending potentials. For water, CO_2, and H_2S molecules, bond-stretching and bond-bending coefficients are set to 1000 $\mathrm{kcal\,\AA^{-2}}$ and 1000 kcal, respectively (see Tables S9 and S10 of the Supplementary Material for the functional forms of these potentials). For the Lennard-Jones (LJ) and bonded (bonds, angles, and dihedrals) interactions of MDEA, $MDEAH^+$, HCO_3^-, and SH^-, the OPLS-AA force field [67,68] is utilized. We used two sets of parameters for the N–C–C–O dihedral of MDEA as the parameters for this dihedral are not available in the OPLS-AA force field: (1) the parameters from Cornell et al. [69] and (2) the parameters from Orozco et al. [70]. The difference in the development of the parameters from Cornell et al. [69] and Orozco et al. [70] is that the first one was parameterized for proteins, nucleic acids, and organic molecules, while the latter was parameterized for alkanolamines by adjusting the densities, vapor pressures, excess enthalpies, and viscosities of six different alkanolamines which is more relevant to the system of our interest.

The point charges of MDEA, $MDEAH^+$, HCO_3^-, and SH^- molecules are computed using quantum chemical calculations performed with Gaussian09 [71] with the 6-311+G(2d,2p) basis set at the second order Møller-Plesset perturbation (MP2) [72] level of theory, by means of a Natural bond orbital (NBO) analysis [73,74]. To obtain accurate densities for aqueous MDEA solutions, the point charges of MDEA molecules are scaled by 0.9 after comparison with experimental data from literature, in line with the previous work on the effect of the scaled charges on transport properties of molecules/ions [2,75–78]. Note that the charge scaling factor validated for aqueous alkanolamine solutions can be used to obtain accurate densities and viscosities of pure alkanolamine solutions as shown in our previous study [2]. To obtain accurate densities and viscosities for CO_2/H_2S-loaded aqueous MDEA solutions, we scaled the point charges of the reaction products from CO_2 ($MDEAH^+$ and HCO_3^-) and H_2S ($MDEAH^+$ and SH^-) absorption by 0.90 and 0.75, respectively. The point charges of water, CO_2, and H_2S are not scaled. For this purpose, we use a scaling factor χ_j^i, where i shows the parameter that is scaled and j represents the specific

Table 1
Number of MDEA and water molecules in MD simulations for different concentrations of MDEA in aqueous MDEA solutions. The average simulation box sizes are computed at 313 K and 1 bar.

MDEA concentration/[wt.%]	Number of MDEA molecules	Number of water molecules	Average box size/[Å]
0	0	700	27.6
10	12	688	28.4
20	25	675	29.4
30	43	657	30.1
40	64	636	31.5
50	92	608	32.6

interaction or molecule for the scaling. For example, a scaling factor of $\chi^q_{\mathrm{MDEA}} = 0.9$ means that the point charges of MDEA molecule were scaled (multiplied) by 0.9. Note that there are more fundamental methods to adjust the point charges (and therefore the dipole moment) of the molecules with point charges computed by quantum chemistry such as the Quantum Mechanical Bespoke approach [79], the Polarization-Consistent Approach [79], and the Self-Consistent Electrostatic Embedding approach [80]. However, in this work, we adopted scaling the point charges of the molecules as it has been shown to produce accurate self-diffusivities [2,47,48,81–83] and to be consistent with our previous work [2]. All force field parameters are tabulated in the Supplementary Material (Tables S1–S21 of the Supplementary Material).

The LJ interactions of unlike atom types are computed using the Lorentz–Berthelot mixing rules [84] unless specified otherwise. In all MD simulations, the LJ interactions are truncated at 12 Å and analytic tail corrections [85] are applied to energies and pressures. Electrostatic interactions are computed using the Particle-Particle Particle-Mesh (PPPM) method with a relative precision of 10^{-5}. The 1–4 LJ and electrostatic intramolecular interactions are scaled by a factor of 0.5 [67,68].

The initial configurations for MD simulations were generated by randomly inserting molecules in a cubic simulation box with a size of 45–55 Å, depending on the MDEA concentration in the solution. The number of molecules of water and MDEA for all systems studied are shown in Table 1. The composition of the simulation box for the acid gas-loaded 50 wt% MDEA/water solutions at 313 K is computed using CASpy [86], an open-source software for computing speciation at reaction equilibrium that we recently developed. To this purpose, we followed the procedure explained in Ref. [86] and computed the composition in CO_2-loaded 50 wt% MDEA/water solutions and H_2S-loaded 50 wt% MDEA/water solutions using the correlations for experimental reaction equilibrium constants reported by Plakia et al. [87]. The compositions of the simulation box of CO_2-loaded 50 wt% MDEA/water solution and H_2S-loaded 50 wt% MDEA/water solutions at 313 K are reported in Tables S22 and S23 of the Supplementary Material.

To compute the self-diffusivities of CO_2 or H_2S, two solute molecules are used to improve statistics. Although two molecules of free CO_2 or H_2S are higher than the solubility of CO_2 or H_2S in the aqueous MDEA solutions [86], we did not encounter any agglomeration of these species in the time period of our MD simulations. Note that the computed self-diffusion coefficients of the acid gases are practically equal to transport diffusion coefficients since CO_2 and H_2S are at the infinite dilution limit [88]. We start the MD simulations with an equilibration stage of 0.5 ns with a timestep of 1 fs in the *NPT* ensemble. The Nosé-Hoover thermostat (with a coupling constant of 10 fs) and barostat (with a coupling constant of 1000 fs) are used to maintain constant temperature and pressure, respectively. Consecutively, another equilibration stage of 1 ns with a timestep of 1 fs is performed in the *NVT* ensemble. Finally, production runs of 20 ns are performed in the *NVE* ensemble to compute all properties of interest.

The On-the-Fly Calculation of Transport Properties (OCTP) plugin [89] in LAMMPS is used to compute viscosities, self-diffusivities, and center-of-mass radial distribution functions (RDFs). The OCTP plugin [89] computes transport properties with the order-*n* [84,90] algorithm using Einstein relations. The center-of-mass RDFs computed by the OCTP plugin are corrected for finite-size effects [89]. For details about these computations the reader is referred to Ref. [89]. In this work, all reported self-diffusivities are corrected for finite-size effects using [91–94]:

$$D_i = D_i^{\mathrm{MD}} + \frac{\xi k_{\mathrm{B}} T}{6\pi\eta L} \tag{1}$$

where D_i is the self-diffusivity of species i at the thermodynamic limit, D_i^{MD} is the self-diffusivity of species i computed from the MD simulation, ξ is a constant equal to 2.837297 for a cubic simulation box, k_{B} is the Boltzmann constant, T is the absolute temperature, η is the viscosity computed from the MD simulation, and L is the length of the simulation box. Note that the computed viscosities do not show any finite-size effects [91,92,95]. The standard deviations for densities, viscosities, and self-diffusion coefficients are computed from seven independent simulations each one starting from a different initial configuration. The average values and uncertainties shown in this work are computed from five independent simulations. Average number of hydrogen bonds between water-MDEA and MDEA-MDEA pairs are computed using VMD Hydrogen Bonds plugin [96] with a cutoff distance of 3.5 Å and a cutoff angle of 30° [97]. To quantify the agreement between the computed values (of density, viscosity, and diffusivity) and experimental values from literature, the coefficient of determination (R^2) scores are computed using:

$$R^2 = 1 - \frac{\sum_{i=1}^{n}(y_{i,\mathrm{exp}} - y_{i,\mathrm{sim}})^2}{\sum_{i=1}^{n}(y_{i,\mathrm{exp}} - \bar{y}_{\mathrm{exp}})^2} \tag{2}$$

where n is the number of data points, $y_{i,\mathrm{exp}}$ is the experimental value from literature, $y_{i,\mathrm{sim}}$ is the computed value, and $\bar{y}_{\mathrm{exp}}$ is the arithmetic average of the experimental values from literature. An R^2 score of 1 means that the agreement between simulations and experiments is perfect.

3. Results and discussion

3.1. Densities and viscosities of aqueous MDEA solutions

To validate the force fields for water, CO_2, and H_2S, we first compute the diffusion coefficients of CO_2 (D_{CO_2}) and H_2S (D_{H_2S}) in pure water. Fig. S3 of the Supplementary Material shows the comparison between the computed and experimental [98,99] self-diffusivities D_{CO_2} and D_{H_2S} in pure water as a function of temperature. Our results show that the computed values of D_{CO_2} and D_{H_2S} in pure water are in excellent agreement with the experimental results from literature [98,99] as the maximum deviations are 12% and 10% for D_{CO_2} and D_{H_2S}, respectively. This shows that the force fields chosen for CO_2, H_2S, and water accurately describe the interactions in aqueous solutions of CO_2 and H_2S. Therefore, we then proceeded with investigating the accuracy of the OPLS-AA force field [67,68] (with point charges computed by quantum chemistry calculations) for MDEA. We used two different sets of parameters for N–C–C–O dihedrals of MDEA molecule as the parameters for this dihedral are not available in the OPLS-AA force field: (1) from Cornell et al. [69], and (2) from Orozco et al. [70]. The main difference between these two sets of parameters for N–C–C–O dihedral is that the parameters from Cornell et al. [69] was developed for proteins, nucleic acids, and organic molecules, while the parameters from Orozco et al. [70] was developed for alkanolamines. Note that the dihedral reported by Orozco et al. [70] is ca. 2.5 times stiffer (i.e. the barrier for dihedral rotation is 2.5 times higher) than the dihedral reported by Cornell et al. [69] (Fig. S4 of the Supplementary Material). We computed the densities of aqueous MDEA solutions as a function of temperature and MDEA concentration in the solution using $\chi^q_{\mathrm{MDEA}} = 1.0$. Fig. S5 of the Supplementary Material shows the comparison between the computed (with unscaled point charges $\chi^q_{\mathrm{MDEA}} =$

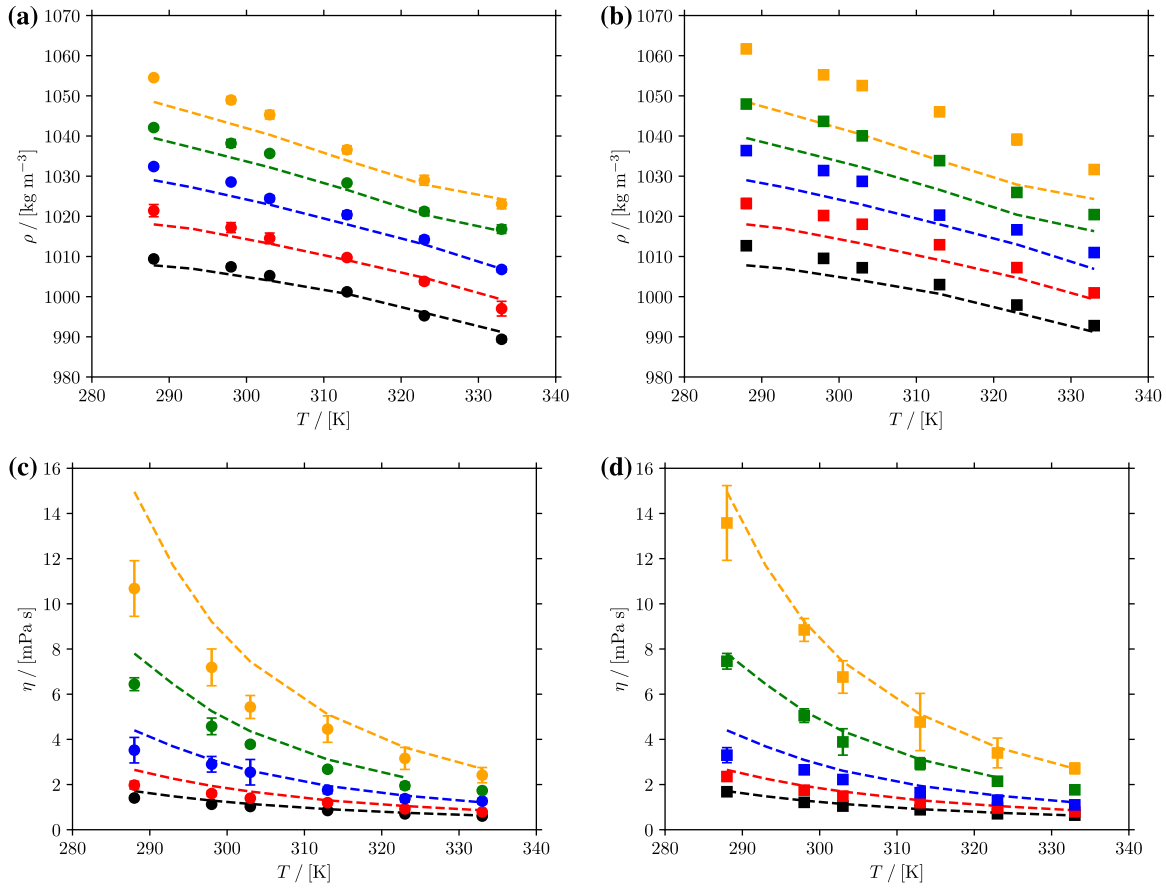

Fig. 1. Computed and experimental [98] (a,b) densities and (c,d) viscosities of aqueous MDEA solutions as a function of temperature at 1 bar. (a,c) show the densities and viscosities computed using the parameters from Cornell et al. [69] for N–C–C–O dihedral of MDEA; (b,d) show the densities and viscosities computed using the N–C–C–O dihedral parameters from Orozco et al. [70]. Note that the point charges of MDEA are scaled with 0.9, i.e. $\chi^q_{\mathrm{MDEA}} = 0.9$. Dashed lines represent experimental results from Al-Ghawas et al. [98]. Color code: black: 10 wt% MDEA/water; red: 20 wt% MDEA/water; blue: 30 wt% MDEA/water; green: 40 wt% MDEA/water; orange: 50 wt% MDEA/water.

1.0) and experimental [98] densities of aqueous MDEA solutions. Our results show that the computed densities are significantly overestimated and the deviations between the computed and experimental densities increase with increasing MDEA concentration in the solution. As it has been shown that the point charges computed using quantum chemical calculations typically overestimate electrostatic interactions and the scaled point charges provide a better representation of the potential energy surface of the molecules/ions [77,100–105], we scaled the point charges of MDEA by 0.9 ($\chi^q_{\mathrm{MDEA}} = 0.9$). Fig. 1 shows the computed and experimental densities of aqueous MDEA solutions (with $\chi^q_{\mathrm{MDEA}} = 0.9$) for the temperature range 288–333 K at 1 bar. Our results show that the computed densities using both sets of parameters for the N–C–C–O dihedral agree very well with the experimental densities from literature [98] with a maximum deviation of 1.3%. The deviation between the experimental data and the computed densities using the parameters from Cornell et al. [69] is 0.1–0.5% (Fig. 1(a)), while the respective deviation is between 0.2–1.3% when the parameters from Orozco et al. [70] are used (Fig. 1(b)). The deviations between the simulations and experimental densities from literature for both dihedral parameters are larger than the standard errors as the standard errors for calculated values of densities are ca. 0.05%. For the dihedral parameters from Orozco et al. [70], the difference between the computed and experimental densities increases with increasing MDEA concentration in the solution. As the densities computed using both set of parameters are in excellent agreement (with a maximum deviation of 1.3%) with experimental data from literature [98], we computed viscosities of aqueous MDEA solutions and compared them with available data from literature.

Fig. 1(c) and Fig. 1(d) show the comparison between the computed (using the same two dihedral parameters discussed earlier) and experimental [98] viscosities of aqueous MDEA solutions for an MDEA concentration range of 10–50 wt% MDEA, and a temperature range of 288–333 K. Our results show that the viscosities computed using both set of parameters for N–C–C–O dihedral underestimate experimental [98] viscosities of aqueous MDEA solutions. The viscosities computed using the parameters from Orozco et al. [70] underestimate experimental results [98] (average absolute deviation of 8.4%) less as the density of aqueous MDEA solutions are higher (due to the 2.5 times stiffer N–C–C–O dihedral, see Fig. S4 of the Supplementary Material) compared to the ones obtained using the parameters from Cornell et al. [69] (average absolute deviation of 13.3%). Note that the average absolute deviation for the viscosities computed using the dihedral parameters from Cornell et al. [69] are larger than the average standard error of 8.3% while the average standard error for viscosities computed using the dihedral parameters from Orozco et al. [70] (8.7%) is slightly higher than the average absolute deviation between simulations and experimental values from literature. To quantify the agreement between the simulations and experimental values from literature, we also computed the R^2 scores. Our findings show that the viscosities computed using the parameters from Cornell et al. [69] for the N–C–C–O dihedral of MDEA and experimental results [98] have an R^2 of 0.88, while the R^2 score of the viscosities computed using N–C–C–O dihedral parameters optimized by Orozco et al. [70] and experimental results [98] is 0.98. Indicatively, the viscosities computed using the N–C–C–O dihedral parameters from Cornell et al. [69] are between 0.6–1.4 mPa s and 2.4–10.7 mPa s at 288–333 K for 10 wt% MDEA/water

and 50 wt% MDEA/water solutions, respectively. The viscosities computed using the N–C–C–O parameters from Orozco et al. [70] vary between 0.6–1.7 mPa s and 2.7–13.6 mPa s at 288–333 K for 10 wt% MDEA/water and 50 wt% MDEA/water solutions, respectively. For the same temperature range, experimental viscosities [98] are between 0.6–1.7 mPa s and 2.7–14.9 mPa s for 10 wt% MDEA/water and 50 wt% MDEA/water solutions, respectively. Both the R^2 scores and deviations from experiments show that the simulations agree well with experiments from literature when the parameters from Orozco et al. [70] for N–C–C–O dihedral are used to predict viscosities of aqueous MDEA solutions.

3.2. Diffusivities of MDEA, CO_2, and H_2S in aqueous MDEA solutions

We further investigate the transport properties of aqueous MDEA solutions by computing the self-diffusion coefficients of MDEA (D_{MDEA}) in the solution. Fig. 2 shows the values of D_{MDEA} computed using the two different sets of parameters for N–C–C–O dihedral for MDEA concentrations in the range of 10-50 wt%, and the comparison with experimental data from Snijder et al. [106] and MD simulation data from Yiannourakou et al. [11] (with the PCFF+ force field reported in ref [107]) for 30 wt% MDEA/water solutions. As expected, our data show that D_{MDEA} decreases with increasing MDEA concentration in the solution (Fig. 2). The values of D_{MDEA} in the 10 wt% MDEA/water solutions are ca. 3 – 9 and 3 – 6 times higher compared to the 50 wt% MDEA/water solutions for the values computed using the parameters from Cornell et al. [69] and Orozco et al. [70], respectively, for the temperature range 288–333 K. Fig. 2(a) shows that the values of D_{MDEA} computed using the parameters from Cornell et al. [69] for the N–C–C–O dihedral are in agreement with the experimental results from Snijder et al. [106] and computational results from Yiannourakou et al. [11] (with an R^2 score of 0.80) for 30 wt% MDEA/water solutions except for the data point at 333 K. The value of D_{MDEA} computed using the parameters from Cornell et al. [69] for N–C–C–O dihedral is 7.94×10^{-10} $\mathrm{m^2\,s^{-1}}$ at 333 K while the experimental value for the same temperature is 9.2×10^{-10} $\mathrm{m^2\,s^{-1}}$. As shown in Fig. 2(b), the values of D_{MDEA} computed using the parameters from Orozco et al. [70] agree very well with the experimental and MD data from literature [11,106] (R^2 score = 0.94). The values of D_{MDEA} computed using the optimized N–C–C–O dihedral parameters from Orozco et al. [70] are between 3.92×10^{-10}–8.89×10^{-10} $\mathrm{m^2\,s^{-1}}$ in 30 wt% MDEA/water solution at 303–333 K, while the experimental values [106] for the same temperature range and solution vary between 4.6×10^{-10}–9.2×10^{-10} $\mathrm{m^2\,s^{-1}}$. This shows that the N–C–C–O dihedral parameters from Orozco et al. [70] perform better than the ones by Cornell et al. [69]. Based on the force field validation for the densities (Fig. 1(a,b)), viscosities (Fig. 1(c,d)) and D_{MDEA}, we hereafter adopt the parameters by Orozco et al. [70] for the N–C–C–O dihedral MDEA to compute the diffusivities of the acid gases in aqueous MDEA solutions.

Interestingly, MDEA diffuses slightly faster in 30 wt% MDEA/water solutions at 333 K ($D_{\mathrm{MDEA}} = 8.89\times10^{-10}$ $\mathrm{m^2\,s^{-1}}$) compared to MEA in 30 wt% MEA/water solutions ($D_{\mathrm{MEA}} = 7.54\times10^{-10}$ $\mathrm{m^2\,s^{-1}}$) from our previous study [2] despite the similar viscosities of both solutions (1.1 mPa s for 30 wt% MDEA/water solutions while 1.2 mPa s for 30 wt% MEA/water solutions [2] at 333 K). Although one would expect the opposite since MEA is smaller and lighter than MDEA (molar mass of MDEA and MEA are 119.163 $\mathrm{g\,mol^{-1}}$ and 61.08 $\mathrm{g\,mol^{-1}}$, respectively), comparing solutions with same alkanolamine weight percentages may be misleading as the mole fractions of these components in these solutions are quite different (mole fraction of MDEA (X_{MDEA}) = 0.06 in 30 wt% MDEA/water solution while mole fraction of MEA (X_{MEA}) = 0.11 in 30 wt% MEA/water solution). Fig. S6 of the Supplementary Material compares D_{MDEA} and D_{MEA} [2] for similar mole fractions of alkanolamine ($X_{\mathrm{MDEA}} = 0.13$ in 50 wt% MDEA/water vs. $X_{\mathrm{MEA}} = 0.11$ in 30 wt% MEA/water solution) in the solution as a function of temperature. Compared to a similar mole fraction of MDEA in MDEA/water solutions, MEA molecules diffuse ca. 2 – 4 times faster in 30 wt% MEA/water solutions than MDEA molecules in 50 wt% MDEA/water solutions for a temperature range of 288 – 333 K.

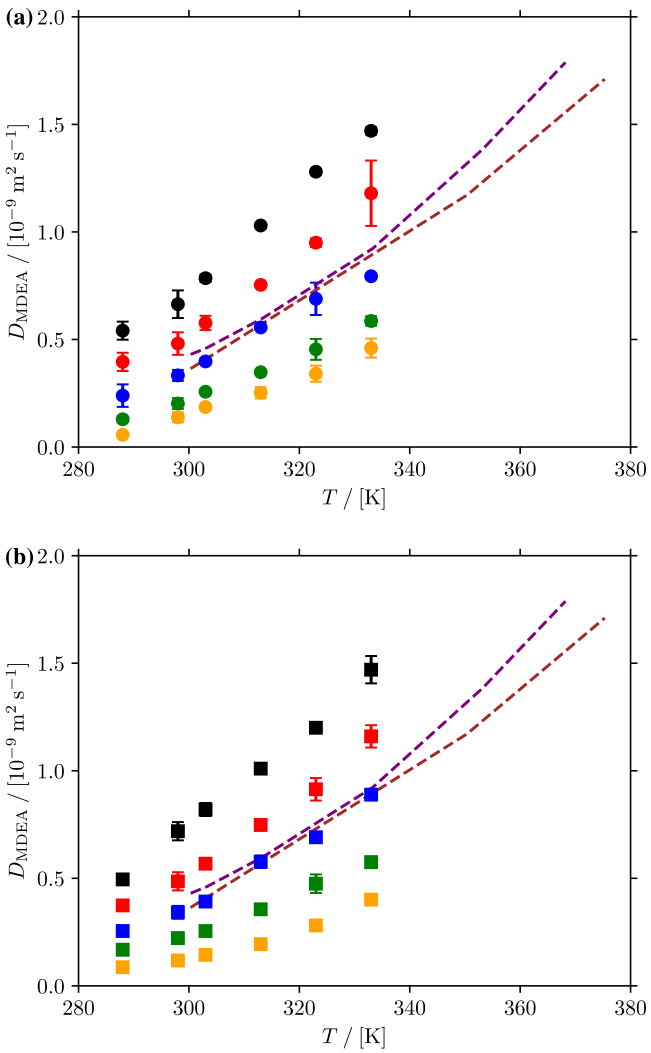

Fig. 2. Computed and experimental [11,106] self-diffusivities D_{MDEA} in aqueous MDEA solutions as a function of temperature at 1 bar. (a) shows the values of D_{MDEA} computed using the parameters from Cornell et al. [69] for N–C–C–O dihedral of MDEA while (b) shows the values of D_{MDEA} computed using the N–C–C–O dihedral from Orozco et al. [70]. Note that the point charges of MDEA are scaled by 0.9, i.e. $\chi^q_{\mathrm{MDEA}} = 0.9$, and all self-diffusivities are corrected for finite-size effects using Eq. (1). Dashed lines represent experimental results in 30 wt% MDEA/water solutions from Snijder et al. [106] (purple) and simulation results from Yiannourakou et al. [11] (brown). The color code follows that of Fig. 1.

We compute the values of $D_{\mathrm{CO_2}}$ and $D_{\mathrm{H_2S}}$ as a function of MDEA concentration in the solution and temperature using MD simulations. Fig. 3 shows the simulation results and comparisons with the available experimental data from literature [98]. To the best of our knowledge, no experimental or modeling data on the diffusivity of H_2S in aqueous MDEA solutions have been reported. Using the CO_2/N_2O analogy [38,39] (by measuring the diffusivity of N_2O), Al-Ghawas et al. [98] estimated the values of $D_{\mathrm{CO_2}}$ to be in the ranges 1.2×10^{-9}–3.1×10^{-9} $\mathrm{m^2\,s^{-1}}$ and 3.8×10^{-10}–1.7×10^{-9} $\mathrm{m^2\,s^{-1}}$ in 10 wt% MDEA/water and 50 wt% MDEA/water solutions, respectively, at temperatures ranging from 288 to 323 K. For the same temperature range, we computed $D_{\mathrm{CO_2}}$ to be 1.29×10^{-9}–2.87×10^{-9} $\mathrm{m^2\,s^{-1}}$ and 3.54×10^{-10}–9.50×10^{-10} $\mathrm{m^2\,s^{-1}}$ in 10 wt% MDEA/water and 50 wt% MDEA/water solutions, respectively. This clearly shows that our data are in agreement with the values of the self-diffusivity of CO_2, $D_{\mathrm{CO_2}}$, estimated using CO_2/N_2O

analogy [98]. Note that Chen et al. [39] investigated the validity of CO_2/N_2O analogy by computing the Henry coefficients and self-diffusivities of CO_2 and N_2O in water, ethanol, n-heptane, and aqueous MEA solutions, and concluded that the assumption holds for 30 wt% MEA/water solutions at 303 K. Also, Kohns et al. [40] stated that the analogy is valid for CO_2 in pure water and ethanol, while it is not valid for CO_2 in binary mixtures of water and ethanol. We also compare the computed values of D_{CO_2} and D_{H_2S} in aqueous MDEA solutions with the ones in aqueous MEA solutions from our previous study [2]. Fig. S7 of the Supplementary Material shows the comparison of D_{CO_2} and D_{H_2S} in aqueous MDEA and aqueous MEA solutions. When solutions with similar mole fractions of MDEA and MEA are compared, CO_2 diffuses ca. 1 – 3 times slower in aqueous MDEA solutions than in aqueous MEA solutions. For example, we computed D_{CO_2} as 5.19×10^{-10}–9.50×10^{-10} $m^2\,s^{-1}$ at 298 – 323 K in 50 wt% MDEA/water solution while the respective value in 30 wt% MEA/water solution at the same temperature range is 1.38×10^{-9}–2.00×10^{-9} $m^2\,s^{-1}$. This is expected since the viscosity of 50 wt% MDEA/water solution is ca. 3 times higher than the viscosity of 30 wt% MEA/water solution at 298 – 323 K and the self-diffusivities of solutes depend highly on the viscosity of the solution. The comparison of the self-diffusivities D_{H_2S} in MEA/water and MDEA/water solutions (Fig. S7(b)) shows a similar difference between the two solutions, i.e. H_2S diffuses ca. 2 times faster in 30 wt% MEA/water solutions than in 50 wt% MDEA/water solutions.

As shown in Fig. 3, the self-diffusivities D_{CO_2} in aqueous MDEA solutions are slightly larger than the self-diffusivities D_{H_2S} at the same conditions. Note that the differences between the computed values of D_{CO_2} and D_{H_2S} are statistically important as the differences are larger than the error bars. H_2S diffuses slower in aqueous MDEA solutions despite its lower molar mass ($M_{H_2S} = 34.1\,g\,mol^{-1}$ vs. $M_{CO_2} = 44.01\,g\,mol^{-1}$) compared to CO_2 because H_2S can form hydrogen bonds with both water and MDEA molecules [2,108–110] and it is a more spherical molecule than CO_2. The values of both D_{CO_2} and D_{H_2S} decrease with increasing MDEA concentration in the solution. For example, both CO_2 and H_2S diffuse ca. 3.5 times faster in 10 wt% MDEA/water solutions than in 50 wt% MDEA/water solutions. Our results also show that the temperature dependency of D_{CO_2} and D_{H_2S} changes significantly with MDEA concentration in the solution. The slope of D_{CO_2} (D_{H_2S}) as a function of temperature is 2.6 (1.8) times higher in 10 wt% MDEA/water solution than in the 50 wt% MDEA/water solution. The same trend can also be seen in the values of D_{CO_2} estimated by Al-Ghawas et al. [98] using the CO_2/N_2O analogy.

The temperature dependence of the self-diffusion coefficients can be described with an Arrhenius equation [2], the Speedy-Angell power equation [111], or the Vogel-Tamann-Fulcher (VTF) equation [112]. We fit the values of D_{CO_2} and D_{H_2S} to an Arrhenius equation [2], the Speedy-Angell power equation [111], and the VTF equation [112] for an MDEA concentration range of 10 – 50 wt% MDEA and a temperature range of 288 – 323 K. The functional forms of these equations are shown in the Supplementary Material. Table 2 and 3 show Arrhenius fit parameters for D_{CO_2} and D_{H_2S}, respectively. The Speedy-Angell and VTF equation fit parameters for D_{CO_2} and D_{H_2S} are tabulated in Tables S24-S27 of the Supplementary Material. Figures S8–S10 of the Supplementary Material show the fits to Arrhenius equation, Speedy-Angell power equation, and VTF equation. The activation energies for diffusion (E_A) for both CO_2 and H_2S increase with MDEA concentration in the solution which also indicates slower diffusion of CO_2 and H_2S with increasing MDEA concentration (see Table 2 and 3).

3.3. Structure of aqueous CO_2/H_2S/MDEA mixtures

In Fig. 4, the center-of-mass RDFs of CO_2 and H_2S with water and MDEA are shown at 313 K and 1 bar. Our findings show that as the MDEA concentration in the solution increases, the first and second peaks in both CO_2-MDEA and H_2S-MDEA RDFs shift to lower values of intermolecular distance, indicating stronger interactions between

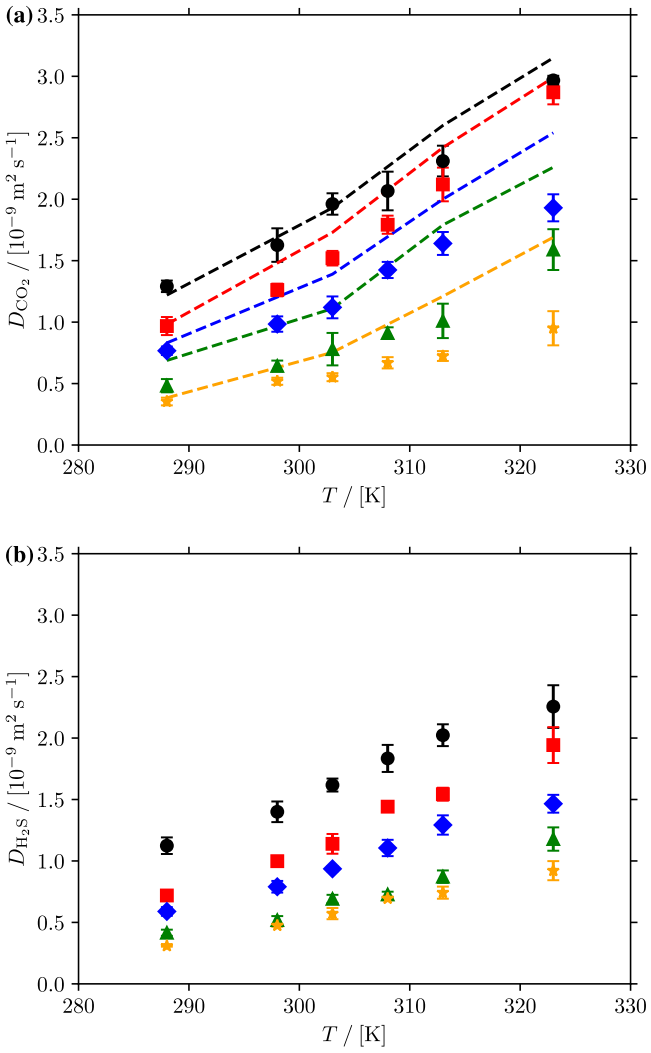

Fig. 3. Computed and experimental [98] (a) self-diffusivities of CO_2 and (b) computed self-diffusivities of H_2S in aqueous MDEA solutions as a function of temperature and MDEA concentration at 1 bar. Note that the point charges of MDEA are scaled with 0.9, i.e. $\chi^q_{MDEA} = 0.9$, and all self-diffusivities are corrected for finite-size effects using Eq. (1). The TraPPE force field [64,65] was used for CO_2 and H_2S. In (a), dashed lines represent experimental results from Al-Ghawas et al. [98]. The color code follows that of Fig. 1.

Table 2
Arrhenius fit parameters (pre-exponential factors (D_0) and activation energies (E_A)) and coefficients of determinations (R^2) for D_{CO_2} in aqueous MDEA solutions with different MDEA concentrations.

MDEA concentration/[wt.%]	D_0/[$m^2\,s^{-1}$]	E_A/[kJ mol^{-1}]	R^2
10	2.71×10^{-6}	18.33	0.991
20	3.51×10^{-5}	25.28	0.997
30	4.97×10^{-6}	21.02	0.975
40	5.78×10^{-5}	28.28	0.981
50	2.25×10^{-6}	20.87	0.991

acid gases and MDEA. However, the intensities of the first peaks in H_2S-MDEA RDFs are higher than those of CO_2-MDEA RDFs, indicating stronger H_2S-MDEA interactions than CO_2-MDEA interactions. The same trend is observed for the CO_2-water and H_2S-water RDFs, where the position of the first and second peaks shift to lower values with increasing MDEA concentration, and the intensities of the first peaks in H_2S-water RDFs are higher than those of CO_2-MDEA RDFs. Overall, these findings suggest that H_2S has stronger interactions with the

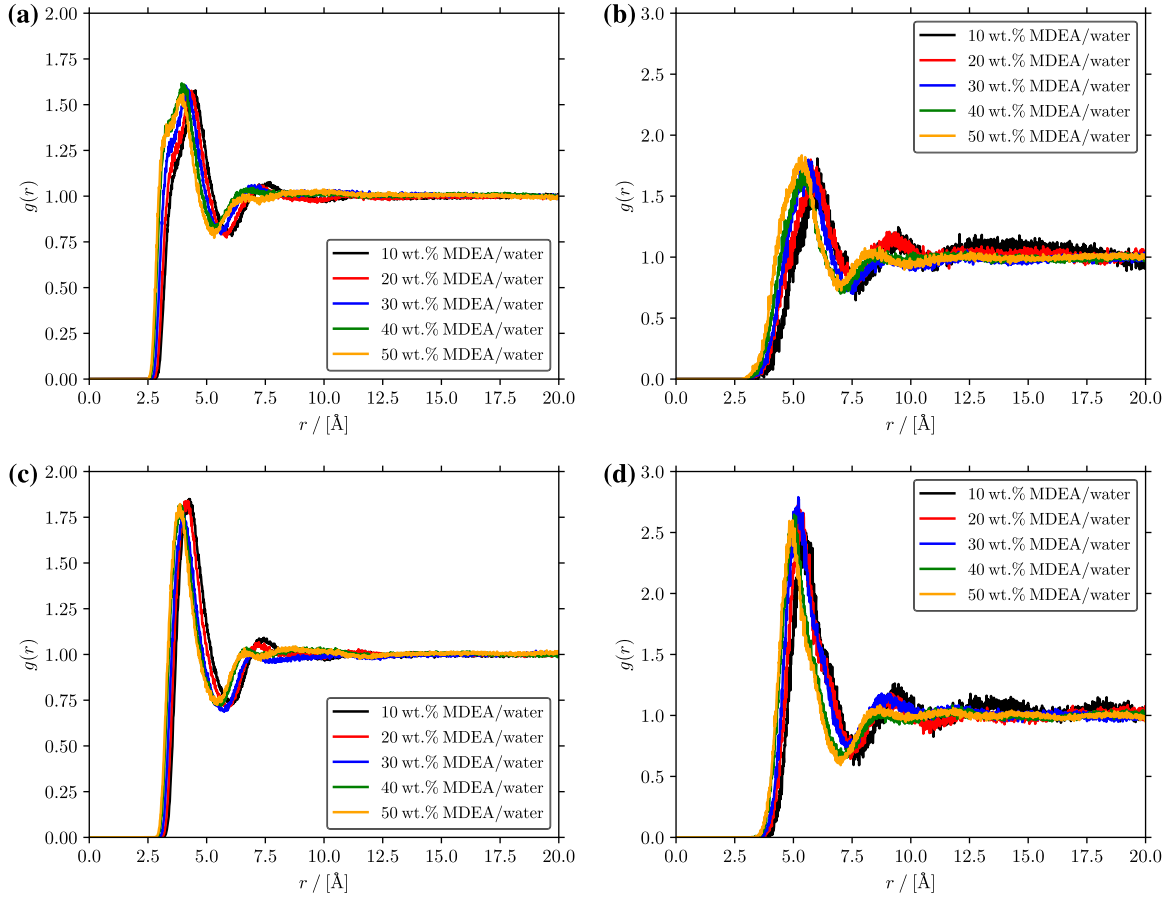

Fig. 4. Radial distribution functions of (a) CO_2–water, (b) CO_2–MDEA, (c) H_2S–water, and (d) H_2S–MDEA at 313 K and 1 bar. For water, the TIP4P/2005 force field [63] was used while for MDEA, we used OPLS-AA force field [67,68] with point charges computed from quantum chemistry. Note that the point charges of MDEA are scaled by 0.9, i.e. $\chi^q_{\text{MDEA}} = 0.9$. For CO_2 and H_2S, the TraPPE force field [64,65] was used.

Table 3
Arrhenius fit parameters (pre-exponential factors (D_0) and activation energies (E_A)) and coefficients of determinations (R^2) for D_{H_2S} in aqueous MDEA solutions with different MDEA concentrations.

MDEA concentration/[wt.%]	D_0/[m^2 s^{-1}]	E_A/[kJ mol^{-1}]	R^2
10	6.79×10^{-7}	15.24	0.976
20	5.59×10^{-6}	21.34	0.986
30	2.34×10^{-6}	19.70	0.972
40	8.82×10^{-6}	23.98	0.988
50	3.04×10^{-6}	21.68	0.973

surrounding molecules (MDEA and water) than CO_2. This is probably the reason why H_2S diffuses slower than CO_2 in aqueous MDEA solutions (Fig. 3). We also compute the average number of hydrogen bonds between water-MDEA and MDEA-MDEA pairs in aqueous MDEA solutions as a function of MDEA concentration at 313 K and 1 bar (Fig. S11 of the Supplementary Material). Our results show that the average number of hydrogen bonds for both water-MDEA and MDEA-MDEA pairs decrease with increasing MDEA concentration in the solution.

3.4. Densities, viscosities, and diffusivities of acid gas-loaded aqueous MDEA solutions

The densities, viscosities, and self-diffusivities of the reaction products are of primary importance in the optimization of the mass transfer in acid gas loaded aqueous MDEA solutions [57–60]. Here, we investigate the densities, viscosities, and self-diffusivities of CO_2 and H_2S loaded aqueous MDEA solutions at 313 K as this is a typical operation temperature in acid gas removal units [32]. We compute the densities of CO_2- or H_2S-loaded 50 wt% MDEA/water solutions at 313 K by using two different scaling factors for the point charges of the reaction products of CO_2 absorption ($MDEAH^+$ and HCO_3^-) and H_2S absorption ($MDEAH^+$ and SH^-), see Tables S23 and S24 of the Supporting Material: $\chi^q_{\text{products}} = 0.90$ and $\chi^q_{\text{products}} = 0.75$. Note that for the point charges of MDEA, we use $\chi^q_{\text{MDEA}} = 0.90$ in all simulations. Fig. 5 shows the comparison between the computed and experimental [113–115] densities of CO_2- and H_2S-loaded 50 wt% MDEA/water solutions at 313 K and 1 bar. Our findings show that the computed densities of CO_2-loaded solutions agree well with the experimental data from literature [113] when the point charges of the reaction products ($MDEAH^+$ and HCO_3^-) are scaled by 0.90. When the point charges of the reaction products ($MDEAH^+$ and HCO_3^-) are scaled by 0.90, the computed densities show an average absolute deviation of 0.8% and a maximum deviation of 1.2%. When a scaling factor of 0.75 is used for the point charges of $MDEAH^+$ and HCO_3^-, the computed densities of CO_2-loaded solutions agree less well with the experimental data [113] with an average absolute deviation of 1.3% and a maximum deviation of 3%. However, following the trend in experimental densities of CO_2-loaded solutions in Fig. 5, it is clear that a scaling factor of 0.9 for the reaction products results in more accurate computed densities than a scaling factor of 0.75 at CO_2 loading of 1 $\text{mol}_{CO_2}\ \text{mol}^{-1}_{\text{amine}}$. The computed densities of H_2S-loaded 50 wt% MDEA/water solutions have average absolute deviations of 3.6% and 1%, and maximum deviations of 4.3% and 2% when scaling factors of $\chi^q_{\text{products}} = 0.90$ and $\chi^q_{\text{products}} = 0.75$ are used, respectively. Our findings show that a scaling factor of $\chi^q_{\text{products}} = 0.90$ results in accurately predicted densities for CO_2-loaded 50 wt% MDEA/water solutions, while the computed densities of H_2S-loaded solution have a better agreement with the experimental data [114,115] when a scaling factor of $\chi^q_{\text{products}} = 0.75$ is used.

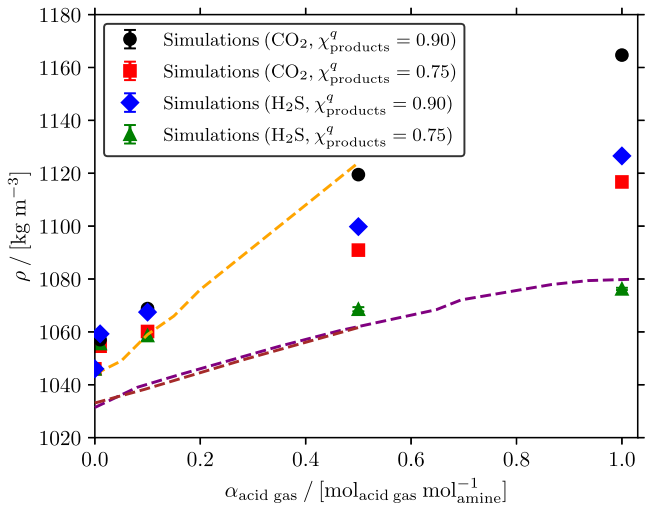

Fig. 5. Densities of acid-gas loaded 50 wt% MDEA/water solutions as a function of acid gas loading at 313 K and 1 bar. The orange dashed line represents experimental densities of CO_2-loaded 50 wt% MDEA solutions from Weiland et al. [113], while the purple and brown dashed lines represent experimental densities of H_2S-loaded 50 wt% MDEA/water solutions from Shoukouhi et al. [114] and Rinker et al. [115], respectively. Note that the point charges of MDEA are scaled by 0.9, i.e. $\chi^q_{MDEA} = 0.9$. The point charges of the reaction products of CO_2 absorption ($MDEAH^+$ and HCO_3^-) and H_2S absorption ($MDEAH^+$ and SH^-) are scaled by either 0.9 or 0.75, i.e. $\chi^q_{products} = 0.9$ or $\chi^q_{products} = 0.75$. For CO_2 and H_2S, the TraPPE force field [64,65] was used.

We compute the viscosities of CO_2 and H_2S-loaded 50 wt% MDEA/water solutions at 313 K and 1 bar using two different scaling factors for the point charges of reaction products from CO_2 and H_2S absorption, $\chi^q_{products} = 0.90$ and $\chi^q_{products} = 0.75$, and compared the computed viscosities with experimental data from literature [114–116]. Fig. 6 shows the comparison between the computed and experimental [114–116] viscosities of acid gas-loaded 50 wt% MDEA/water solutions at 313 K and 1 bar. For CO_2-loaded solutions, our findings show that the computed viscosities agree well with the experimental data from Pinto et al. [116] when a scaling factor of $\chi^q_{products} = 0.90$ is used, capturing the increasing viscosity of the solutions with increasing CO_2 loading. However, the computed viscosities are significantly underestimated when $\chi^q_{products} = 0.75$ is used, especially at high CO_2 loadings. The computed viscosities of H_2S-loaded 50 wt% MDEA/water solutions agree well when a scaling factor of $\chi^q_{products} = 0.75$, while a scaling factor of $\chi^q_{products} = 0.90$ results in significant overestimation of the computed viscosities. Our simulations also capture the effect of slightly decreasing viscosity of the solutions with increasing H_2S loading. Therefore, we decided to compute the self-diffusivities of free CO_2, $MDEAH^+$, and HCO_3^- in CO_2-loaded 50 wt% MDEA/water solutions using a scaling factor of $\chi^q_{products} = 0.90$, while using a scaling factor of $\chi^q_{products} = 0.75$ for the MD simulations of H_2S-loaded solutions. The reason for scaling down the point charges of the reaction products of H_2S absorption (SH^- and $MDEAH^+$) to a greater extent compared to those of the reaction products of CO_2 absorption (HCO_3^- and $MDEAH^+$) may be attributed to quantum chemistry calculations overestimating the electrostatic interactions of SH^- ion more than the electrostatic interactions of HCO_3^- ion. This may be due to the greater polarity of SH^- ion compared to the HCO_3^- ion.

Fig. 7 shows the computed self-diffusivities of free CO_2, free H_2S, and the reaction products of CO_2 or H_2S absorption in 50 wt% MDEA/water solutions at 313 K and 1 bar. To the best of our knowledge, the data of self-diffusivities of the reaction products in CO_2 or H_2S loaded aqueous MDEA solutions reported here are the first in literature. For CO_2-loaded aqueous MDEA solutions, our results show that for free CO_2, HCO_3^-, and $MDEAH^+$, the self-diffusivities show a decreasing trend with increasing CO_2 loading. For all species, the self-diffusivities

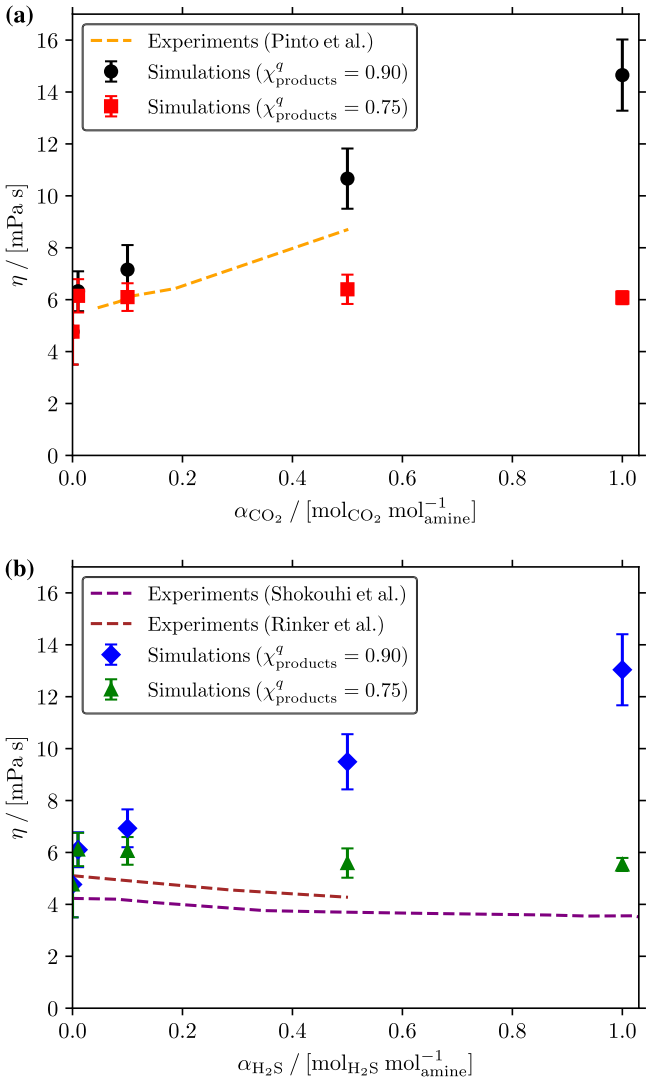

Fig. 6. Comparison of the computed and experimental [114–116] viscosities of (a) CO_2-loaded and (b) H_2S-loaded 50 wt% MDEA/water solutions as a function of acid gas loading at 313 K and 1 bar. Note that the point charges of MDEA are scaled with 0.9, i.e. $\chi^q_{MDEA} = 0.9$. The point charges of the reaction products of CO_2 absorption ($MDEAH^+$ and HCO_3^-) and H_2S absorption ($MDEAH^+$ and SH^-) are scaled by either 0.9 or 0.75, i.e. $\chi^q_{products} = 0.9$ or $\chi^q_{products} = 0.75$. For CO_2 and H_2S, the TraPPE force field [64,65] was used.

in CO_2-loaded 50 wt% MDEA/water solutions decrease by ca. 50% from a CO_2 loading of 0.01 mol_{CO_2} mol^{-1}_{amine} to 1 mol_{CO_2} mol^{-1}_{amine}. This is expected since the viscosities of the CO_2-loaded solutions increase with increasing CO_2 loading (Fig. 6(a)). However, the self-diffusivities of free H_2S, SH^-, and $MDEAH^+$ are not affected by the changes in H_2S loading. The self-diffusivities of H_2S and H_2S related reaction products also follow the same trend as the viscosities of H_2S-loaded 50 wt% MDEA/water solutions (Fig. 6(b)) and the viscosities of H_2S-loaded solutions also showed minimal change with changing H_2S loading. Our results indicate that the absorption of CO_2 slows down with increasing CO_2 loading whereas the absorption of H_2S does not exhibit the same behavior. This may be due the linear shape of the SH^- ion (as opposed to the spherical HCO_3^- ion) and a speculative proposition; a proton hopping mechanism between SH^- and water molecules where the ion acts as a proton hole [117,118].

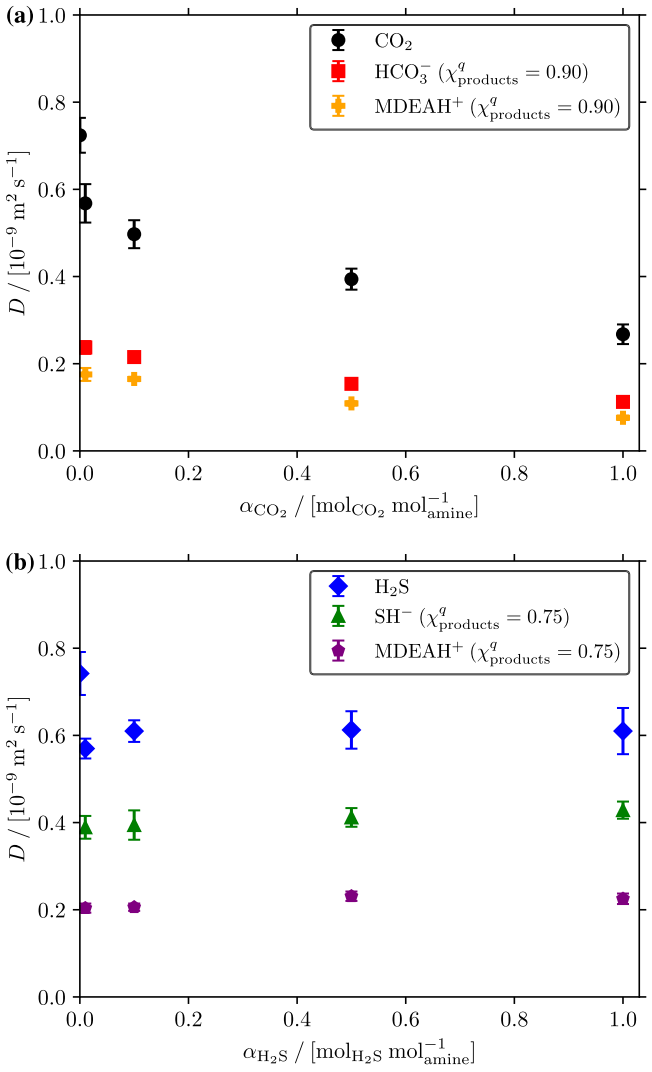

Fig. 7. Self-diffusivities of free acid gases and the reaction products from acid gas absorption in (a) CO_2-loaded and (b) H_2S-loaded 50 wt% MDEA/water solutions as a function of acid gas loading at 313 K and 1 bar. Note that the point charges of MDEA are scaled with 0.9, i.e. $\chi^q_{MDEA} = 0.9$. The point charges of the reaction products of CO_2 absorption ($MDEAH^+$ and HCO_3^-) and H_2S absorption ($MDEAH^+$ and SH^-) are scaled by 0.9 and 0.75, respectively. All self-diffusivities are corrected for finite-size effects using Eq. (1). For CO_2 and H_2S, the TraPPE force field [64,65] was used.

4. Conclusions

In this study, the effects of temperature and MDEA concentration in aqueous MDEA solutions on the values of the self-diffusivities D_{CO_2} and D_{H_2S} were investigated using classical MD simulations. First, we computed the densities of aqueous MDEA solutions for a temperature range of 288 – 333 K and an MDEA concentration of 10 – 50 wt% MDEA using two different sets of parameters for the N–C–C–O dihedral in MDEA, showing excellent agreement with experimental data from literature. We also computed the viscosities of aqueous MDEA solutions and showed that the computed viscosities agree well with experimental results from literature when the dihedral parameters from Orozco et al. [70] and a point charge scaling factor of 0.9 for MDEA are used. To validate that the diffusion of MDEA molecules are accurately captured in the MD simulations, we computed D_{MDEA} in aqueous MDEA solutions for a wide range of temperatures and MDEA concentrations and compared our data with available data in literature, showing a good agreement. Next, we computed D_{CO_2} and D_{H_2S} in aqueous MDEA solutions. Our findings showed that both CO_2 and H_2S diffuse 3.5 times faster in 10 wt% MDEA/water solutions than in 50 wt% MDEA/water solutions and H_2S diffuse slower than CO_2 in aqueous MDEA solutions. We also investigated the RDFs between CO_2, H_2S, water, and MDEA molecules and showed that the interactions between H_2S and the surrounding molecules are stronger than those between CO_2 and the surrounding molecules which explains why H_2S diffuse slower than CO_2 in these solutions. Our results also showed that the interactions between the acid gases and surrounding molecules are stronger with increasing MDEA concentration in the solution. Finally, we investigated the impact of acid gas loading on the densities, viscosities and self-diffusivities (of acid gases and reaction products) in 50 wt% MDEA/water solutions at 313 K and 1 bar. The densities, viscosities, and self-diffusivities in the acid gas loaded aqueous MDEA solutions are important for the modeling of the mass transfer in loaded solutions. Comparing the computed densities and viscosities of CO_2 and H_2S-loaded solutions with experimental data from literature showed that two different point charge scaling factors are needed to accurately compute the densities and viscosities of acid gas-loaded aqueous MDEA solutions. When a scaling factor of 0.90 for the point charges of reaction products of CO_2 absorption (HCO_3^- and $MDEAH^+$) and a scaling factor of 0.75 for those of H_2S absorption (SH^- and $MDEAH^+$) are used, we showed that the viscosities of CO_2-loaded aqueous MDEA solutions increase with increasing CO_2 loading while the viscosities do not show a significant change with changing H_2S loading in H_2S-loaded solutions. For the first time in literature, we computed the self-diffusivities of free CO_2, HCO_3^-, and $MDEAH^+$ in CO_2-loaded 50 wt% MDEA/water solutions, and free H_2S, SH^-, and $MDEAH^+$ in H_2S-loaded 50 wt% MDEA/water solutions at 313 K. Our results showed that the self-diffusivities in CO_2-loaded solutions significantly decrease with increasing CO_2 loading while the self-diffusivities in H_2S-loaded solutions did not change significantly with changing H_2S loading in the solution which indicates that CO_2 absorption slows down with increasing CO_2 loading while this is not the case for H_2S absorption.

CRediT authorship contribution statement

H. Mert Polat: Simulations, Data analysis, Writing of original and revised manuscript. **Casper van der Geest:** Simulations, Data analysis. **Frédérick de Meyer:** Data analysis, Co-supervision of project, Proof-reading of original and revised manuscript. **Céline Houriez:** Data analysis, Co-supervision of project, Proof-reading of original and revised manuscript. **Thijs J.H. Vlugt:** Data analysis, Co-supervision of project, Writing of original and revised manuscript. **Othonas A. Moultos:** Conceptualization, Data curation, Main supervision of the project, Writing of original and revised manuscript.

Declaration of competing interest

The authors declare that they have no known competing financial interests or personal relationships that could have appeared to influence the work reported in this paper.

Data availability

Data will be made available on request.

Acknowledgments

This work was supported by the CO_2 and Sustainability R&D program from TotalEnergies S.E, France. We are grateful for the support by NWO Domain Science for the use of supercomputer facilities, with financial support from the Nederlandse Organisatie voor Wetenschappelijk Onderzoek (Netherlands Organisation for Scientific Research, NWO). The authors acknowledge the use of computational resources of DelftBlue supercomputer, provided by Delft High Performance Computing Centre (https://www.tudelft.nl/dhpc).

Appendix A. Supplementary data

Supplementary material related to this article can be found online at https://doi.org/10.1016/j.fluid.2023.113913.

References

[1] F.-Y. Liang, M. Ryvak, S. Sayeed, N. Zhao, The role of natural gas as a primary fuel in the near future, including comparisons of acquisition, transmission and waste handling costs of as with competitive alternatives, Chem. Central J. 6 (2012) S4.

[2] H.M. Polat, F. de Meyer, C. Houriez, C. Coquelet, O.A. Moultos, T.J.H. Vlugt, Transport properties of mixtures of acid gases with aqueous monoethanolamine solutions: A molecular dynamics study, Fluid Phase Equilib. 564 (2023) 113587.

[3] J.H. Ausubel, A. Grübler, N. Nakicenovic, Carbon dioxide emissions in a methane economy, Clim. Change 12 (1988) 245–263.

[4] F. Holz, P.M. Richter, R. Egging, A global perspective on the future of natural gas: Resources, trade, and climate constraints, Rev. Environ. Econ. Policy 9 (2015) 85–106.

[5] A. Safari, N. Das, O. Langhelle, J. Roy, M. Assadi, Natural gas: A transition fuel for sustainable energy system transformation? Energy Sci. Eng. 7 (2019) 1075–1094.

[6] C. Gürsan, V. de Gooyert, The systemic impact of a transition fuel: Does natural gas help or hinder the energy transition? Renew. Sustain. Energy Rev. 138 (2021) 110552.

[7] L. Barelli, G. Bidini, F. Gallorini, S. Servili, Hydrogen production through sorption-enhanced steam methane reforming and membrane technology: A review, Energy 33 (2008) 554–570.

[8] R. Davarnejad, B. Rahimi, S.N. Baghban, M.A. Khansary, A.H. Sani, Development of a thermodynamic model for hydrogen and hydrogen containing mixtures, Fluid Phase Equilib. 382 (2014) 1–9.

[9] X.-H. Wang, H.-B. Qin, A. Dandekar, Y.-F. Wang, Y.-F. Sun, Q.-L. Ma, B. Liu, L.-Y. Yang, C.-Y. Sun, G.-J. Chen, Hydrate phase equilibrium of $H_2/CH_4/CO_2$ ternary gas mixtures and cage occupancy percentage of hydrogen molecules, Fluid Phase Equilib. 403 (2015) 160–166.

[10] M. Momirlan, T. Veziroglu, Current status of hydrogen energy, Renew. Sustain. Energy Rev. 6 (2002) 141–179.

[11] M. Yiannourakou, X. Rozanska, B. Minisini, F. de Meyer, Molecular simulations for improved process modeling of an acid gas removal unit, Fluid Phase Equilib. 560 (2022) 113478.

[12] W.F. Burgers, P.S. Northrop, H.S. Kheshgi, J.A. Valencia, Worldwide development potential for sour gas, in: Energy Procedia, vol. 4, Elsevier Ltd, 2011, pp. 2178–2184.

[13] G. Kang, Z.P. Chan, S.B.M. Saleh, Y. Cao, Removal of high concentration CO_2 from natural gas using high pressure membrane contactors, Int. J. Greenhouse Gas Control 60 (2017) 1–9.

[14] G.M. Dlamini, P.L. Fosbøl, N. von Solms, Modelling phase equilibria of sulphur compounds in mixtures relevant to carbon capture and storage with new association schemes, Fluid Phase Equilib. 568 (2023) 113738.

[15] J. Jiang, A. Chan, S. Ali, A. Saha, K.J. Haushalter, W.-L.M. Lam, M. Glasheen, J. Parker, M. Brenner, S.B. Mahon, H.H. Patel, R. Ambasudhan, S.A. Lipton, R.B. Pilz, G.R. Boss, Hydrogen sulfide—Mechanisms of toxicity and development of an antidote, Sci. Rep. 6 (2016) 20831.

[16] S. Mokhatab, W.A. Poe, J.Y. Mak, Chapter 4 - basic concepts of natural gas processing, in: S. Mokhatab, W.A. Poe, J.Y. Mak (Eds.), Handbook of Natural Gas Transmission and Processing (Fourth Edition), Fourth Edition, Gulf Professional Publishing, 2019, pp. 177–189.

[17] G. George, N. Bhoria, S. Alhallaq, A. Abdala, V. Mittal, Polymer membranes for acid gas removal from natural gas, Sep. Purif. Technol. 158 (2016) 333–356.

[18] D. Turi, M. Ho, M. Ferrari, P. Chiesa, D. Wiley, M. Romano, CO_2 capture from natural gas combined cycles by CO_2 selective membranes, Int. J. Greenhouse Gas Control 61 (2017) 168–183.

[19] K. Maqsood, A. Mullick, A. Ali, K. Kargupta, S. Ganguly, Cryogenic carbon dioxide separation from natural gas: A review based on conventional and novel emerging technologies, Rev. Chem. Eng. 30 (2014).

[20] K.-H. Park, J.W. Lee, Y. Lim, Y. Seo, Life cycle cost analysis of CO_2 compression processes coupled with a cryogenic distillation unit for purifying high-CO_2 natural gas, J. CO_2 Util. 60 (2022) 102002.

[21] J.S. Eow, Recovery of sulfur from sour acid gas: A review of the technology, Environ. Prog. 21 (2002) 143–162.

[22] Y. Wei, L. Wang, Y. Yang, L. Wen, X. Huo, L. Zhang, M. Yang, Molecular mechanism in the solubility reduction of elemental sulfur in H_2S/CH_4 mixtures: A molecular modeling study, Fluid Phase Equilib. 569 (2023) 113764.

[23] A. Haghtalab, M. Mohammadi, Z. Fakhroueian, Absorption and solubility measurement of CO_2 in water-based ZnO and SiO_2 nanofluids, Fluid Phase Equilib. 392 (2015) 33–42.

[24] R.L. Siegelman, P.J. Milner, E.J. Kim, S.C. Weston, J.R. Long, Challenges and opportunities for adsorption-based CO_2 capture from natural gas combined cycle emissions, Energy Environ. Sci. 12 (2019) 2161–2173.

[25] H.M. Polat, M. Zeeshan, A. Uzun, S. Keskin, Unlocking CO_2 separation performance of ionic liquid/CuBTC composites: Combining experiments with molecular simulations, Chem. Eng. J. 373 (2019) 1179–1189.

[26] T. Rufford, S. Smart, G. Watson, B. Graham, J. Boxall, J.D. da Costa, E. May, The removal of CO_2 and N_2 from natural gas: A review of conventional and emerging process technologies, J. Pet. Sci. Eng. 94–95 (2012) 123–154.

[27] E. Skylogianni, I. Mundal, D.D. Pinto, C. Coquelet, H.K. Knuutila, Hydrogen sulfide solubility in 50 wt% and 70 wt% aqueous methyldiethanolamine at temperatures from 283 to 393 K and total pressures from 500 to 10000 kPa, Fluid Phase Equilib. 511 (2020).

[28] L. Guo, Y. Wang, B. Wang, N. Wang, L. Zhang, Y. Chen, A simplified semi-empirical model for modeling of CO_2 solubilities in aqueous MDEA and MEA solutions, Fluid Phase Equilib. 555 (2022) 113352.

[29] C. Mathonat, V. Majer, A. Mather, J.-P. Grolier, Enthalpies of absorption and solubility of CO_2 in aqueous solutions of methyldiethanolamine, Fluid Phase Equilib. 140 (1997) 171–182.

[30] S. Bishnoi, G.T. Rochelle, Absorption of carbon dioxide in aqueous piperazine/methyldiethanolamine, AIChE J. 48 (2002) 2788–2799.

[31] S. Moioli, L.A. Pellegrini, P. Vergani, F. Brignoli, Study of the robustness of a low-temperature dual-pressure process for removal of CO_2 from natural gas, Front. Chem. Sci. Eng. 12 (2018) 209–225.

[32] A.A. Orlov, A. Valtz, C. Coquelet, X. Rozanska, E. Wimmer, G. Marcou, D. Horvath, B. Poulain, A. Varnek, F.D. Meyer, Computational screening methodology identifies effective solvents for CO_2 capture, Commun. Chem. 5 (2022) 1–7.

[33] L. Peters, A. Hussain, M. Follmann, T. Melin, M.-B. Hägg, CO_2 removal from natural gas by employing amine absorption and membrane technology—A technical and economical analysis, Chem. Eng. J. 172 (2011) 952–960.

[34] U.S.P.R. Arachchige, M.C. Melaaen, Aspen plus simulation of CO_2 removal from coal and gas fired power plants, Energy Procedia 23 (2012) 391–399.

[35] A. Muhammad, Y. GadelHak, Correlating the additional amine sweetening cost to acid gases load in natural gas using Aspen HYSYS, J. Nat. Gas Sci. Eng. 17 (2014) 119–130.

[36] N.M. Al-Lagtah, S. Al-Habsi, S.A. Onaizi, Optimization and performance improvement of Lekhwair natural gas sweetening plant using Aspen HYSYS, J. Nat. Gas Sci. Eng. 26 (2015) 367–381.

[37] S. Dara, A.S. Berrouk, Computer-based optimization of acid gas removal unit using modified CO_2 absorption kinetic models, Int. J. Greenhouse Gas Control 59 (2017) 172–183.

[38] G.F. Versteeg, W.P.M.V. Swaaij, Solubility and diffusivity of acid gases (carbon dioxide, nitrous oxide) in aqueous alkanolamine solutions, J. Chem. Eng. Data 33 (1988) 29–34.

[39] Q. Chen, S.P. Balaji, M. Ramdin, J.J. Gutiérrez-Sevillano, A. Bardow, E. Goetheer, T.J.H. Vlugt, Validation of the CO_2/N_2O analogy using molecular simulation, Ind. Eng. Chem. Res. 53 (2014) 18081–18090.

[40] M. Kohns, S. Werth, M. Horsch, E. von Harbou, H. Hasse, Molecular simulation study of the CO_2-N_2O analogy, Fluid Phase Equilib. 442 (2017) 44–52.

[41] E. Sada, H. Kumazawa, M.A. Butt, Solubility and diffusivity of gases in aqueous solutions of amines, J. Chem. Eng. Data 23 (1978) 161–163.

[42] J.J. Ko, T.C. Tsai, C.Y. Lin, H.M. Wang, M.H. Li, Diffusivity of nitrous oxide in aqueous alkanolamine solutions, J. Chem. Eng. Data 46 (2001) 160–165.

[43] J. Ying, D.A. Eimer, Measurements and correlations of diffusivities of nitrous oxide and carbon dioxide in monoethanolamine + water by laminar liquid jet, Ind. Eng. Chem. Res. 51 (2012) 16517–16524.

[44] D.T. Kallikragas, A.Y. Plugatyr, I.M. Svishchev, High temperature diffusion coefficients for O_2, H_2, and OH in water, and for pure water, J. Chem. Eng. Data 59 (6) (2014) 1964–1969.

[45] O.A. Moultos, I.N. Tsimpanogiannis, A.Z. Panagiotopoulos, J.P.M. Trusler, I.G. Economou, Atomistic molecular dynamics simulations of carbon dioxide diffusivity in *n*-hexane, *n*-decane, *n*-hexadecane, cyclohexane, and squalane, J. Phys. Chem. B 120 (50) (2016) 12890–12900.

[46] X. Zhao, H. Jin, Y. Chen, Z. Ge, Numerical study of H_2, CH_4, CO, O_2 and CO_2 diffusion in water near the critical point with molecular dynamics simulation, Comput. Math. Appl. 81 (2021) 759–771.

[47] P. Habibi, A. Rahbari, S. Blazquez, C. Vega, P. Dey, T.J.H. Vlugt, O.A. Moultos, A new force field for OH^- for computing thermodynamic and transport properties of H_2 and O_2 in aqueous NaOH and KOH solutions, J. Phys. Chem. B 126 (45) (2022) 9376–9387.

[48] W.A. van Rooijen, P. Habibi, K. Xu, P. Dey, T.J.H. Vlugt, H. Hajibeygi, O.A. Moultos, Interfacial tensions, solubilities, and transport properties of the H_2/H_2O/NaCl system: A molecular simulation study, J. Chem. Eng. Data (2023) http://dx.doi.org/10.1021/acs.jced.2c00707, in press.

[49] O.A. Moultos, I.N. Tsimpanogiannis, A.Z. Panagiotopoulos, I.G. Economou, Atomistic molecular dynamics simulations of CO_2 diffusivity in H_2O for a wide range of temperatures and pressures, J. Phys. Chem. B 118 (2014) 5532–5541.

[50] O.A. Moultos, I.N. Tsimpanogiannis, A.Z. Panagiotopoulos, I.G. Economou, Self-diffusion coefficients of the binary (H_2O + CO_2) mixture at high temperatures and pressures, J. Chem. Thermodyn. 93 (2016) 424–429.

[51] G.A. Orozco, V. Lachet, A.D. Mackie, Physical absorption of green house gases in amines: The influence of functionality, structure, and cross-interactions, J. Phys. Chem. B 120 (2016) 13136–13143.

[52] A. Rendón-Calle, G.A. Orozco, S. Builes, Predictions of fluidities of amines by molecular simulations: TraPPE-EH vs. OPLS-AA, Fluid Phase Equilib. 464 (2018) 40–46.

[53] I.N. Tsimpanogiannis, O.A. Moultos, L.F. Franco, M.B.d.M. Spera, M. Erdős, I.G. Economou, Self-diffusion coefficient of bulk and confined water: A critical review of classical molecular simulation studies, Mol. Simul. 45 (4–5) (2019) 425–453.

[54] L.E. Castro-Anaya, G.A. Orozco, Self-diffusion coefficients of amines, a molecular dynamics study, Fluid Phase Equilib. 553 (2022) 113301.

[55] S.M. Melnikov, M. Stein, Molecular dynamics study of the solution structure, clustering, and diffusion of four aqueous alkanolamines, J. Phys. Chem. B 122 (2018) 2769–2778.

[56] S. Mokhatab, W.A. Poe, Chapter 7 - natural gas sweetening, in: S. Mokhatab, W.A. Poe (Eds.), Handbook of Natural Gas Transmission and Processing (Second Edition), second ed., Gulf Professional Publishing, Boston, 2012, pp. 253–290.

[57] R. Littel, B. Filmer, G. Versteeg, W.V. Swaaij, Modelling of simultaneous absorption of H_2S and CO_2 in alkanolamine solutions: The influence of parallel and consecutive reversible reactions and the coupled diffusion of ionic species, Chem. Eng. Sci. 46 (1991) 2303–2313.

[58] M.A. Pacheco, G.T. Rochelle, Rate-based modeling of reactive absorption of CO_2 and H_2S into aqueous methyldiethanolamine, Ind. Eng. Chem. Res. 37 (1998) 4107–4117.

[59] M.E. Adams, T.L. Marshall, R.L. Rowley, Diffusion coefficients significant in modeling the absorption rate of carbon dioxide into aqueous blends of *N*-methyldiethanolamine and diethanolamine and of hydrogen sulfide into aqueous *N*-methyldiethanolamine, J. Chem. Eng. Data 43 (1998) 605–610.

[60] Y. Yu, T. Zhang, G. Liu, Z. Zhang, G. Wang, Identifying the multi-ion effects on the phase flow, mass and heat transfer in amine absorption of CO_2, Int. J. Heat Mass Transfer 114 (2017) 501–516.

[61] S. Plimpton, Fast parallel algorithms for short-range molecular dynamics, J. Comput. Phys. 117 (1995) 1–19.

[62] Delft High Performance Computing Centre (DHPC), DelftBlue supercomputer (phase 1), 2022, https://www.tudelft.nl/dhpc/ark:/44463/DelftBluePhase1.

[63] J.L.F. Abascal, C. Vega, A general purpose model for the condensed phases of water: TIP4P/2005, J. Chem. Phys. 123 (2005) 234505.

[64] J.J. Potoff, J.I. Siepmann, Vapor–liquid equilibria of mixtures containing alkanes, carbon dioxide, and nitrogen, AIChE J. 47 (2001) 1676–1682.

[65] M.S. Shah, M. Tsapatsis, J.I. Siepmann, Development of the transferable potentials for phase equilibria model for hydrogen sulfide, J. Phys. Chem. B 119 (2015) 7041–7052.

[66] G.A. Orozco, I.G. Economou, A.Z. Panagiotopoulos, Optimization of intermolecular potential parameters for the CO_2/H_2O mixture, J. Phys. Chem. B 118 (2014) 11504–11511.

[67] W.L. Jorgensen, D.S. Maxwell, J. Tirado-Rives, Development and testing of the OPLS all-atom force field on conformational energetics and properties of organic liquids, J. Am. Chem. Soc. 118 (1996) 11225–11236.

[68] R.C. Rizzo, W.L. Jorgensen, OPLS all-atom model for amines: Resolution of the amine hydration problem, J. Am. Chem. Soc. 121 (1999) 4827–4836.

[69] W.D. Cornell, P. Cieplak, C.I. Bayly, I.R. Gould, K.M. Merz, D.M. Ferguson, D.C. Spellmeyer, T. Fox, J.W. Caldwell, P.A. Kollman, A second generation force field for the simulation of proteins, nucleic acids, and organic molecules, J. Am. Chem. Soc. 117 (1995) 5179–5197.

[70] G.A. Orozco, V. Lachet, C. Nieto-Draghi, A.D. MacKie, A transferable force field for primary, secondary, and tertiary alkanolamines, J. Chem. Theory Comput. 9 (2013) 2097–2103.

[71] M.J. Frisch, G.W. Trucks, H.B. Schlegel, G.E. Scuseria, M.A. Robb, J.R. Cheeseman, G. Scalmani, V. Barone, B. Mennucci, G.A. Petersson, H. Nakatsuji, M. Caricato, X. Li, H.P. Hratchian, A.F. Izmaylov, J. Bloino, G. Zheng, J.L. Sonnenberg, M. Hada, M. Ehara, K. Toyota, R. Fukuda, J. Hasegawa, M. Ishida, T. Nakajima, Y. Honda, O. Kitao, H. Nakai, T. Vreven, J.A. Montgomery, J.E. Peralta, F. Ogliaro, M. Bearpark, J.J. Heyd, E. Brothers, K.N. Kudin, V.N. Staroverov, R. Kobayashi, J. Normand, K. Raghavachari, A. Rendell, J.C. Burant, S.S. Iyengar, J. Tomasi, M. Cossi, N. Rega, J.M. Millam, M. Klene, J.E. Knox, J.B. Cross, V. Bakken, C. Adamo, J. Jaramillo, R. Gomperts, R.E. Stratmann, O. Yazyev, A.J. Austin, R. Cammi, C. Pomelli, J.W. Ochterski, R.L. Martin, K. Morokuma, V.G. Zakrzewski, G.A. Voth, P. Salvador, J.J. Dannenberg, S. Dapprich, A.D. Daniels, Ö. Farkas, J.B. Foresman, J.V. Ortiz, J. Cioslowski, D.J. Fox, Gaussian 09 revision e.01, 2009, Gaussian Inc. Wallingford CT.

[72] C. Møller, M.S. Plesset, Note on an approximation treatment for many-electron systems, Phys. Rev. 46 (1934) 618–622.

[73] J.P. Foster, F. Weinhold, Natural hybrid orbitals, J. Am. Chem. Soc. 102 (1980) 7211–7218.

[74] A.E. Reed, L.A. Curtiss, F. Weinhold, Intermolecular interactions from a natural bond orbital, donor-acceptor viewpoint, Chem. Rev. 88 (1988) 899–926.

[75] B.L. Bhargava, S. Balasubramanian, Refined potential model for atomistic simulations of ionic liquid [bmim][PF_6], J. Chem. Phys. 127 (2007) 114510.

[76] T.G.A. Youngs, C. Hardacre, Application of static charge transfer within an ionic-liquid force field and its effect on structure and dynamics, ChemPhysChem 9 (2008) 1548–1558.

[77] S.L. Perkins, P. Painter, C.M. Colina, Experimental and computational studies of choline chloride-based deep eutectic solvents, J. Chem. Eng. Data 59 (2014) 3652–3662.

[78] A.T. Celebi, T.J.H. Vlugt, O.A. Moultos, Structural, thermodynamic, and transport properties of aqueous reline and ethaline solutions from molecular dynamics simulations, J. Phys. Chem. B 123 (2019) 11014–11025.

[79] M. Jorge, M.C. Barrera, A.W. Milne, C. Ringrose, D.J. Cole, What is the optimal dipole moment for nonpolarizable models of liquids? J. Chem. Theory Comput. 19 (2023) 1790–1804.

[80] M. Jorge, J.R. Gomes, M.C. Barrera, The dipole moment of alcohols in the liquid phase and in solution, J. Mol. Liq. 356 (2022) 119033.

[81] H.S. Salehi, A.T. Celebi, T.J.H. Vlugt, O.A. Moultos, Thermodynamic, transport, and structural properties of hydrophobic deep eutectic solvents composed of tetraalkylammonium chloride and decanoic acid, J. Chem. Phys. 154 (2021) 144502.

[82] A.L. Benavides, M.A. Portillo, V.C. Chamorro, J.R. Espinosa, J.L.F. Abascal, C. Vega, A potential model for sodium chloride solutions based on the TIP4P/2005 water model, J. Chem. Phys. 147 (2017) 104501.

[83] A.Z. Panagiotopoulos, Simulations of activities, solubilities, transport properties, and nucleation rates for aqueous electrolyte solutions, J. Chem. Phys. 153 (2020) http://dx.doi.org/10.1063/5.0012102.

[84] D. Frenkel, B. Smit, Understanding Molecular Simulation: From Algorithms to Applications, Vol. 1, second ed., Academic Press, San Diego, California, 2002.

[85] M.P. Allen, D.J. Tildesley, Computer Simulation of Liquids, second ed., Oxford University Press, Oxford, UK, 2017.

[86] H.M. Polat, F. de Meyer, C. Houriez, O.A. Moultos, T.J.H. Vlugt, Solving chemical absorption equilibria using free energy and quantum chemistry calculations: Methodology, limitations, and new open-source software, J. Chem. Theory Comput. 19 (2023) 2616–2629.

[87] A. Plakia, E. Voutsas, Modeling of H_2S, CO_2+H_2S, and CH_4+CO_2 solubilities in aqueous monoethanolamine and methyldiethanolamine solutions, Ind. Eng. Chem. Res. 59 (2020) 11317–11328.

[88] T. Janzen, J. Vrabec, Diffusion coefficients of a highly nonideal ternary liquid mixture: Cyclohexane–toluene–methanol, Ind. Eng. Chem. Res. 57 (2018) 16508–16517.

[89] S.H. Jamali, L. Wolff, T.M. Becker, M. de Groen, M. Ramdin, R. Hartkamp, A. Bardow, T.J.H. Vlugt, O.A. Moultos, OCTP: A tool for on-the-fly calculation of transport properties of fluids with the Order-n algorithm in LAMMPS, J. Chem. Inf. Model. 59 (2019) 1290–1294.

[90] D. Dubbeldam, D.C. Ford, D.E. Ellis, R.Q. Snurr, A new perspective on the order-*n* algorithm for computing correlation functions, Mol. Simul. 35 (2009) 1084–1097.

[91] I.-C. Yeh, G. Hummer, System-size dependence of diffusion coefficients and viscosities from molecular dynamics simulations with periodic boundary conditions, J. Phys. Chem. B 108 (2004) 15873–15879.

[92] S.H. Jamali, L. Wolff, T.M. Becker, A. Bardow, T.J.H. Vlugt, O.A. Moultos, Finite-size effects of binary mutual diffusion coefficients from molecular dynamics, J. Chem. Theory Comput. 14 (2018) 2667–2677.

[93] S.H. Jamali, A. Bardow, T.J.H. Vlugt, O.A. Moultos, Generalized form for finite-size corrections in mutual diffusion coefficients of multicomponent mixtures obtained from equilibrium molecular dynamics simulation, J. Chem. Theory Comput. 16 (2020) 3799–3806.

[94] A.T. Celebi, S.H. Jamali, A. Bardow, T.J.H. Vlugt, O.A. Moultos, Finite-size effects of diffusion coefficients computed from molecular dynamics: A review of what we have learned so far, Mol. Simul. 47 (2021) 831–845.

[95] O.A. Moultos, Y. Zhang, I.N. Tsimpanogiannis, I.G. Economou, E.J. Maginn, System-size corrections for self-diffusion coefficients calculated from molecular dynamics simulations: The Case of CO_2, n-alkanes, and Poly(Ethylene Glycol) Dimethyl Ethers, J. Chem. Phys. 145 (7) (2016) 074109.

[96] W. Humphrey, A. Dalke, K. Schulten, VMD – Visual molecular dynamics, J. Mol. Graph. 14 (1996) 33–38.

[97] A. Luzar, D. Chandler, Effect of environment on hydrogen bond dynamics in liquid water, Phys. Rev. Lett. 76 (1996) 928–931.

[98] H.A. Al-Ghawas, D.P. Hagewiesche, G. Ruiz-Ibanez, O.C. Sandall, Physicochemical properties important for carbon dioxide absorption in aqueous methyldiethanolamine, J. Chem. Eng. Data 34 (1989) 385–391.

[99] N. Haimour, O.C. Sandall, Molecular diffusivity of hydrogen sulfide in water, J. Chem. Eng. Data 29 (1984) 20–22.

[100] A.T. Celebi, N. Dawass, O.A. Moultos, T.J.H. Vlugt, How sensitive are physical properties of choline chloride-urea mixtures to composition changes: Molecular dynamics simulations and Kirkwood-Buff theory, J. Chem. Phys. 154 (2021) 184502.

[101] V.V. Chaban, I.V. Voroshylova, O.N. Kalugin, A new force field model for the simulation of transport properties of imidazolium-based ionic liquids, Phys. Chem. Chem. Phys. 13 (2011) 7910–7920.

[102] H. Liu, E. Maginn, A.E. Visser, N.J. Bridges, E.B. Fox, Thermal and transport properties of six ionic liquids: An experimental and molecular dynamics study, Ind. Eng. Chem. Res. 51 (2012) 7242–7254.

[103] S.L. Perkins, P. Painter, C.M. Colina, Molecular dynamic simulations and vibrational analysis of an ionic liquid analogue, J. Phys. Chem. B 117 (2013) 10250–10260.

[104] S. Blazquez, I.M. Zeron, M.M. Conde, J.L. Abascal, C. Vega, Scaled charges at work: Salting out and interfacial tension of methane with electrolyte solutions from computer simulations, Fluid Phase Equilib. 513 (2020) 112548.
[105] S. Blazquez, M.M. Conde, C. Vega, Scaled charges for ions: An improvement but not the final word for modeling electrolytes in water, J. Chem. Phys. 158 (2023) 054505.
[106] E.D. Snijder, M.J. te Riele, G.F. Versteeg, W.P. van Swaaij, Diffusion coefficients of several aqueous alkanolamine solutions, J. Chem. Eng. Data 38 (1993) 475–480.
[107] H. Sun, COMPASS: An ab initio force-field optimized for condensed-phase applications – Overview with details on alkane and benzene compounds, J. Phys. Chem. B 102 (1998) 7338–7364.
[108] X. Song, Y. Zhang, C. Wu, X. Sheng, H. Zhao, Exploration of H_2S capture by alkanolamines, Struct. Chem. 30 (2019) 2419–2428.
[109] Monu, B.K. Oram, B. Bandyopadhyay, Bridging H_2O and H_2S homomeric clusters via H_2O-H_2S mixed clusters: Impact of the changing ratio of H_2O and H_2S moieties, Comput. Theor. Chem. 1213 (2022) 113740.
[110] T.C. Chan, H.T. Li, K.Y. Li, Effects of shapes of solute molecules on diffusion: A study of dependences on solute size, solvent, and temperature, J. Phys. Chem. B 119 (2015) 15718–15728.
[111] R.J. Speedy, C.A. Angell, Isothermal compressibility of supercooled water and evidence for a thermodynamic singularity at -45° C, J. Chem. Phys. 65 (1976) 851–858.
[112] W. Lu, H. Guo, I.M. Chou, R.C. Burruss, L. Li, Determination of diffusion coefficients of carbon dioxide in water between 268 and 473K in a high-pressure capillary optical cell with in situ Raman spectroscopic measurements, Geochim. Cosmochim. Acta 115 (2013) 183–204.
[113] R.H. Weiland, J.C. Dingman, D.B. Cronin, Heat capacity of aqueous monoethanolamine, diethanolamine, *N*-methyldiethanolamine, and *N*-ethyldiethanolamine-based blends with carbon dioxide, J. Chem. Eng. Data 42 (1997) 1004–1006.
[114] M. Shokouhi, R. Ahmadi, Measuring the density and viscosity of H_2S-loaded aqueous methyldiethanolamine solution, J. Chem. Thermodyn. 102 (2016) 228–236.
[115] E.B. Rinker, A.T. Colussi, N.L. McKnight, O.C. Sandall, Effect of hydrogen sulfide loading on the density and viscosity of aqueous solutions of methyldiethanolamine, J. Chem. Eng. Data 45 (2000) 254–256.
[116] D.D.D. Pinto, B. Johnsen, M. Awais, H.F. Svendsen, H.K. Knuutila, Viscosity measurements and modeling of loaded and unloaded aqueous solutions of MDEA, DMEA, DEEA and MAPA, Chem. Eng. Sci. 171 (2017) 340–350.
[117] D. Riccardi, P. König, X. Prat-Resina, H. Yu, M. Elstner, T. Frauenheim, Q. Cui, "Proton holes" in long-range proton transfer reactions in solution and enzymes: A theoretical analysis, J. Am. Chem. Soc. 128 (2006) 16302–16311.
[118] T. Miyake, M. Rolandi, Grotthuss mechanisms: From proton transport in proton wires to bioprotonic devices, J. Phys.: Condens. Matter 28 (2016) 023001.

Supplementary Material for: Densities, Viscosities, and Diffusivities of Loaded and Unloaded Aqueous CO_2/H_2S/MDEA Mixtures: A Molecular Dynamics Simulation Study

H. Mert Polat[a], Casper van der Geest[a], Frédérick de Meyer[b,c], Céline Houriez[c], Thijs J. H. Vlugt[a], Othonas A. Moultos[a,*]

[a] *Engineering Thermodynamics, Process & Energy Department, Faculty of Mechanical Engineering, Delft University of Technology, Leeghwaterstraat 39, Delft 2628CB, The Netherlands*

[b] *CO_2 and Sustainability R&D Program, Gas & Low Carbon Entity, OneTech, TotalEnergies S.E., 92078 Paris, France*

[c] *Mines Paris, PSL University, Center for Thermodynamics of Processes (CTP), 77300 Fontainebleau, France*

[*] Corresponding author

Email address: o.moultos@tudelft.nl (Othonas A. Moultos)

Preprint submitted to Fluid Phase Equilibria *July 22, 2023*

The following items are presented in this Supplementary Material:

- Functional forms of the Arrhenius, Speedy-Angell and Vogel-Tamann-Fulcher (VTF) equations (section S1),
- Force field parameters used in MD simulations (Tables S1–S22),
- Compositions of the simulation boxes used in the MD simulations of CO_2 and H_2S-loaded aqueous MDEA simulations (Tables S23 and S24),
- Speedy-Angell and VTF fit parameters for the self-diffusivities D_{CO_2} and D_{H_2S} in aqueous MDEA solutions (Tables S25–S28),
- Computed and experimental [1, 2] self-diffusivities D_{CO_2} and D_{H_2S} in pure water as a function of temperature (Figure S3),
- Dihedral potential energy as a function of dihedral angle for the N–C–C–O dihedral in MDEA for the dihedral parameters from Cornell et al. [3] and Orozco et al. [4] (Figure S4),
- Computed and experimental [1] densities of aqueous MDEA solutions as a function of temperature and MDEA concentration with $\chi^q_{MDEA} = 1$ (Figure S5),
- Comparison between the self-diffusivities of MDEA in 50 wt.% MDEA/water solutions and MEA in 30 wt.% MEA/water solutions as a function of temperature (Figure S6),
- Comparison between the self-diffusivities D_{CO_2} and D_{H_2S} in aqueous MDEA solutions and 30 wt.% MEA/water solutions (Figure S7),
- Computed values of the self-diffusivities D_{CO_2} and D_{H_2S} as a function of temperature and MDEA concentration, and the fits to the Arrhenius, Speedy-Angell and VTF equations, respectively (Figures S8, S9, and S10).

S1. Arrhenius, Speedy-Angell Power, and Vogel-Tamann-Fulcher Equations

We fit the values of D_{CO_2} and D_{H_2S} in aqueous MDEA solutions to the Arrhenius equation, the Speedy-Angell power equation [5], and the Vogel-Tamann-Fulcher (VTF) equation [6]. The Arrhenius equation equals:

$$D_{\text{self}} = D_0 \exp\left[-\frac{E_A}{RT}\right] \tag{S1}$$

where D_{self} is the self-diffusion coefficient, D_0 is the pre-exponential factor, T is the absolute temperature, R is the ideal gas constant, and E_A is the activation energy for diffusion. The Speedy-Angell power equation equals:

$$D_{\text{self}} = D_0 \left(\frac{T}{T_s} - 1\right)^m \tag{S2}$$

where T_s is the singularity temperature and m is a fit parameter. We also fit the values of D_{CO_2} and D_{H_2S} to the VTF equation using:

$$D_{\text{self}} = \exp\left[\frac{-\alpha}{T - \beta} - \gamma\right] \tag{S3}$$

where α, β, and γ are fit parameters.

Table S1: The atom types and coordinates of the TraPPE [7] CO_2 molecule.

Atom type	x / [Å]	y / [Å]	z / [Å]
C	1.16	0.00	0.00
O	0.00	0.00	0.00
O	2.32	0.00	0.00

Table S2: Force field parameters for carbon dioxide. The TraPPE [7] force field was used for carbon dioxide.

Atom	ϵ/k_B / [K]	σ / [Å]	q / [e^-]
O	79.0	3.05	-0.35
C	27.0	2.80	0.70

Table S3: The atom types and coordinates of the TraPPE [8] H_2S molecule.

Atom type	x / [Å]	y / [Å]	z / [Å]
S	0.0000000	0.0000000	0.0000000
H	1.3400000	0.0000000	0.0000000
H	-0.0467526	1.3391826	0.0000000

Table S4: Force field parameters for hydrogen sulfide. The TraPPE [8] force field was used for hydrogen sulfide.

Atom	ϵ/k_B / [K]	σ / [Å]	q / [e^-]
S	125.0	3.60	-0.28
H	50.0	2.50	0.14

Table S5: The atom types and coordinates of the TIP4P/2005 [9] water molecule. The atom type M represents the dummy charge site in the TIP4P/2005 force field.

Atom type	x / [Å]	y / [Å]	z / [Å]
O	0.00000000	0.00000000	0.00000000
H	-0.75695033	0.58588228	0.00000000
H	0.75695033	0.58588228	0.00000000
M	0.00000000	0.15000000	0.00000000

Table S6: Force field parameters for water. The TIP4P/2005 [9] force field was used for water.

Atom	ϵ/k_B / [K]	σ / [Å]	q / [e^-]
O	81.899	3.16435	0.00000
H	0.0000	0.00000	0.52422
M	0.0000	0.00000	-1.04844

Table S7: Non-bonded interaction parameters between CO_2 and water. The optimized potential developed by Orozco et al. [10] was used.

Atoms	ϵ/k_B / [K]	σ / [Å]
$O_{CO_2} - O_{H_2O}$	79.14	3.058
$C_{CO_2} - O_{H_2O}$	53.04	3.052

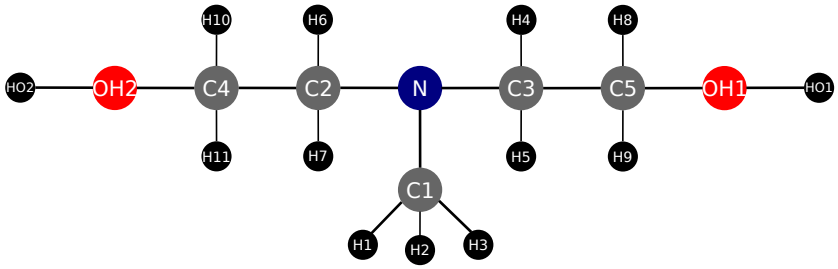

Figure S1: Schematic representation showing the atom type designation of MDEA. Color code: black: hydrogen; blue: nitrogen; red: oxygen; grey: carbon.

Table S8: Intermolecular force field parameters for MDEA. The OPLS-AA force field [11, 12] with point charges computed by quantum chemical calculations (MP2/6-311+G(2d,2p)) was used for MDEA. The point charges listed in this table are unscaled charges, i.e. $\chi^q_{\mathrm{MDEA}} = 1.0$. The tabulated point charges sum up to zero. As explained in the main text, in our simulations, these point charges are scaled by $\chi^q_{\mathrm{MDEA}} = 0.9$. The atom labels are defined in Fig. S1.

Atom	ϵ/k_{B} / [K]	σ / [Å]	q / [e^-]
N	85.47	3.30	-0.63525
C1	33.18	3.50	-0.26080
C2	33.18	3.50	-0.10893
C3	33.18	3.50	-0.11385
C4	33.18	3.50	0.06446
C5	33.18	3.50	0.06972
OH1	85.47	3.12	-0.78207
OH2	85.47	3.12	-0.77757
H1	15.08	2.50	0.16784
H2	15.08	2.50	0.16269
H3	15.08	2.50	0.14238
H4	15.08	2.50	0.17381
H5	15.08	2.50	0.15235
H6	15.08	2.50	0.17490
H7	15.08	2.50	0.14150
H8	7.54	2.50	0.12994
H9	7.54	2.50	0.12320
H10	7.54	2.50	0.12901
H11	7.54	2.50	0.12130
HO1	0.50	1.00	0.46226
HO2	0.50	1.00	0.46311

Table S9: Harmonic bond stretching potential parameters for MDEA. The OPLS-AA [11, 12] force field is used for MDEA. To compute the bonding potentials, we use $U_{\text{bond}} = K(r - r_0)^2$ where K is the bond coefficient, r is the distance between two atoms, and r_0 is the equilibrium distance between two atoms. The atom labels are defined in Fig. S1.

Bond	r_0 / [Å]	K/k_{B} / [K Å^{-2}]
C–C	1.529	134735.7
C–H	1.090	170933.4
C–N	1.448	192048.7
C–O	1.410	160878.5
O–H	0.960	278018.2

Table S10: Harmonic bond bending angle potential parameters for MDEA. The OPLS-AA [11, 12] force field is used for MDEA. To compute the angle potentials, we use $U_{\text{angle}} = K(\theta - \theta_0)^2$ where K is the bending strength, θ is the bending angle between three atoms, and θ_0 is the equilibrium bending angle. The atom labels are defined in Fig. S1.

Angle	θ_0 / [°]	K/k_{B} / [K]
C–C–H	110.70	18852.9
C–C–N	109.47	28254.3
C–C–O	109.50	25137.3
C–O–H	108.50	27651.0
H–C–H	107.80	16590.6
H–C–N	109.50	17596.1
H–C–O	109.50	25137.3

Table S11: OPLS-AA dihedral potential parameters for MDEA. The OPLS-AA [11, 12] force field is used for the dihedrals in MDEA, except for the N–C–C–O dihedral. For the N–C–C–O dihedral, we either use the parameters reported by Cornell et al. [3] or Orozco et al. [4]. To compute the dihedral potential for the dihedrals in this table, we use $U_{\text{dihedral}} = \frac{1}{2}K_1\left[1 + \cos(\phi)\right] + \frac{1}{2}K_2\left[1 - \cos(2\phi)\right] + \frac{1}{2}K_3\left[1 + \cos(3\phi)\right] + \frac{1}{2}K_4\left[1 - \cos(4\phi)\right]$ where $K_1..K_4$ are the dihedral coefficients and ϕ is the dihedral angle. The values of K_4 are 0 for all dihedrals listed in this table. The atom labels are defined in Fig. S1.

Dihedral	K_1/k_{B} / [K]	K_2/k_{B} / [K]	K_3/k_{B} / [K]
H–C–N–C [11, 12]	0.00	0.00	281.54
C–N–C–C [11, 12]	209.14	-64.35	349.41
C–C–O–H [11, 12]	-178.98	-87.48	247.35
N–C–C–O [3]	0.00	0.00	1407.69

Table S12: The optimized parameters for N–C–C–O dihedral from Orozco et al. [4]. All energies in this table are divided by the Boltzmann constant k_B and reported in units of K. To compute the dihedral potential for the N–C–C–O dihedral with the parameters in this table, we use $U_{\text{dihedral}} = \sum_{i=1,9} \left[a_i cos^{i-1}(\phi)\right]$ where $a_1..a_9$ are the dihedral coefficients and ϕ is the dihedral angle. The atom labels are defined in Fig. S1.

Dihedral	a_1/k_B	a_2/k_B	a_3/k_B	a_4/k_B	a_5/k_B	a_6/k_B	a_7/k_B	a_8/k_B	a_9/k_B
N–C–C–O	57.00	5889.99	1231.11	-9428.99	-6584.23	14567.26	6614.81	-11345.20	2511.20

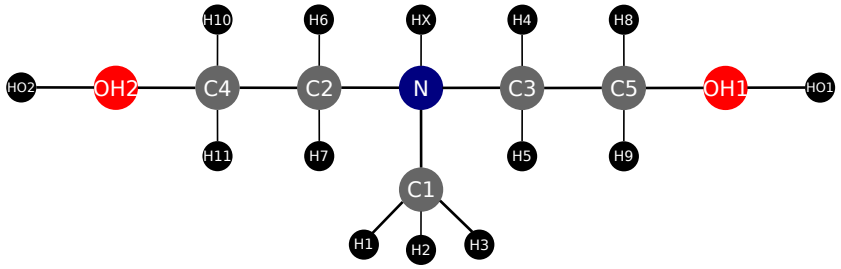

Figure S2: Schematic representation showing atom type designations of $MDEAH^+$. Color code: black: hydrogen; blue: nitrogen; red: oxygen; grey: carbon.

Table S13: Intermolecular force field parameters for $MDEAH^+$. The OPLS-AA force field [11, 12] with point charges computed by quantum chemical calculations (MP2/6-311+G(2d,2p)) was used for $MDEAH^+$. The point charges listed in this table are unscaled charges, i.e. $\chi^q_{\mathrm{MDEAH^+}} = 1.0$. The tabulated point charges sum up to exactly 1. As explained in the main text, in our simulations, these point charges are scaled by 0.90 or 0.75. The atom labels are defined in Fig. S2.

Atom	ϵ/k_B / [K]	σ / [Å]	q / [e^-]
N	85.47	3.25	-0.47548
C1	33.18	3.50	-0.30317
C2	33.18	3.50	-0.14067
C3	33.18	3.50	-0.13852
C4	33.18	3.50	-0.00517
C5	33.18	3.50	-0.00620
OH1	85.47	3.12	-0.76945
OH2	85.47	3.12	-0.76864
H1	15.08	2.50	0.21511
H2	15.08	2.50	0.20877
H3	15.08	2.50	0.20350
H4	15.08	2.50	0.20965
H5	15.08	2.50	0.20554
H6	15.08	2.50	0.20990
H7	15.08	2.50	0.20690
H8	15.08	2.50	0.18279
H9	15.08	2.50	0.15767
H10	15.08	2.50	0.18284
H11	15.08	2.50	0.15725
HO1	1.00	1.00	0.49508
HO2	1.00	1.00	0.49556
HX	1.00	1.00	0.47674

Table S14: Harmonic bond stretching potential parameters for $MDEAH^+$. The OPLS-AA [11, 12] force field is used for $MDEAH^+$. To compute the bonding potentials, we use $U_{\text{bond}} = K(r - r_0)^2$ where K is the bond coefficient, r is the distance between two atoms, and r_0 is the equilibrium distance between two atoms. The atom labels are defined in Fig. S2.

Bond	r_0 / [Å]	K/k_{B} / [K Å^{-2}]
C–C	1.529	134735.7
C–H	1.090	170933.4
C–N	1.471	184507.5
C–O	1.410	160878.5
O–H	0.945	278018.2
N–H	1.01	218191.5

Table S15: Harmonic bond bending angle potential parameters for $MDEAH^+$. The OPLS-AA [11, 12] force field is used for $MDEAH^+$. To compute the angle potentials, we use $U_{\text{angle}} = K(\theta - \theta_0)^2$ where K is the bending strength, θ is the bending angle between three atoms, and θ_0 is the equilibrium bending angle. The atom labels are defined in Fig. S2.

Angle	θ_0 / [°]	K/k_{B} / [K]
C–C–H	110.70	18852.9
C–C–N	111.20	40219.6
C–C–O	109.50	25137.3
C–O–H	108.50	27651.0
C–N–C	113.00	25137.3
C–N–H	107.64	16163.3
H–C–H	107.80	16590.6
H–C–N	109.50	17596.1
H–C–O	109.50	17596.1

Table S16: OPLS-AA dihedral potential parameters for $MDEAH^+$. The OPLS-AA [11, 12] force field is used for the dihedrals in $MDEAH^+$ except for the N–C–C–O dihedral. For the N–C–C–O dihedral, we used the parameters reported by Orozco et al. [4] (Table S12). To compute the dihedral potential for the dihedrals in this table, we use $U_{\text{dihedral}} = \frac{1}{2}K_1\left[1+\cos(\phi)\right]+\frac{1}{2}K_2\left[1-\cos(2\phi)\right]+\frac{1}{2}K_3\left[1+\cos(3\phi)\right]+\frac{1}{2}K_4\left[1-\cos(4\phi)\right]$ where $K_1..K_4$ are the dihedral coefficients and ϕ is the dihedral angle. The values of K_4 are 0 for all dihedrals listed in this table. The atom labels are defined in Fig. S2.

Dihedral	K_1/k_B / [K]	K_2/k_B / [K]	K_3/k_B / [K]
C–C–O–H	-178.98	-87.48	247.35
C–N–C–C	722.95	-62.34	132.72
H–C–N–C	0.00	0.00	151.83
N–C–C–H	0.00	0.00	193.05
H–C–N–H	0.00	0.00	131.22
H–C–O–H	0.00	0.00	176.97
H–C–C–O	0.00	0.00	235.28
H–N–C–C	0.00	0.00	174.45
H–C–C–H	0.00	0.00	150.82

Table S17: Intermolecular force field parameters for HCO_3^-. The OPLS-AA force field [11, 12] with point charges computed by quantum chemical calculations (MP2/6-311+G(2d,2p)) was used for HCO_3^-. The point charges listed in this table are unscaled charges, i.e. $\chi^q_{HCO_3^-} = 1.0$. The tabulated point charges sum up to exactly -1. As explained in the main text, in our simulations, these point charges are scaled by 0.90 or 0.75. The atom labels are as follows: C: carbon of HCO_3^-; O1: oxygen connected to carbon in HCO_3^-; O2: oxygen connected to carbon in HCO_3^-; OH: oxygen of OH group in HCO_3^-; HO: hydrogen of OH group in HCO_3^-.

Atom	ϵ/k_B / [K]	σ / [Å]	q / [e^-]
C	35.190	3.55	1.15070
O1	105.58	2.96	-0.90698
O2	105.58	2.96	-0.86222
OH	85.470	3.12	-0.83705
HO	1.0000	1.00	0.45555

Table S18: Harmonic bond stretching potential parameters for HCO_3^-. The OPLS-AA [11, 12] force field is used for HCO_3^-. To compute the bonding potentials, we use $U_{\text{bond}} = K(r - r_0)^2$ where K is the bond coefficient, r is the distance between two atoms, and r_0 is the equilibrium distance between two atoms. The atom labels are designated in the caption of Table S17.

Bond	r_0 / [Å]	K/k_{B} / [K Å^{-2}]
C–O	1.250	329800.9
C–OH	1.364	226235.4
OH-HO	0.945	278018.2

Table S19: Harmonic bond bending angle potential parameters for HCO_3^-. The OPLS-AA [11, 12] force field is used for HCO_3^-. To compute the angle potentials, we use $U_{\text{angle}} = K(\theta - \theta_0)^2$ where K is the bending strength, θ is the bending angle between three atoms, and θ_0 is the equilibrium bending angle. The atom labels are designated in the caption of Table S17.

Angle	θ_0 / [°]	K/k_{B} / [K]
O–C–OH	121	40219.6
O–C–O	126	40219.6
C–OH–HO	113	17596.1

Table S20: OPLS-AA dihedral potential parameters for HCO_3^-. The OPLS-AA [11, 12] force field is used for the dihedrals in HCO_3^-. To compute the dihedral potential for the dihedrals in this table, we use $U_{\text{dihedral}} = \frac{1}{2}K_1[1 + \cos(\phi)] + \frac{1}{2}K_2[1 - \cos(2\phi)] + \frac{1}{2}K_3[1 + \cos(3\phi)] + \frac{1}{2}K_4[1 - \cos(4\phi)]$ where $K_1..K_4$ are the dihedral coefficients and ϕ is the dihedral angle. The values of K_4 are 0 for all dihedrals listed in this table. The atom labels are designated in the caption of Table S17.

Dihedral	K_1/k_{B} / [K]	K_2/k_{B} / [K]	K_3/k_{B} / [K]
O–C–OH–HO	0.0	2765.1	0.0

Table S21: Intermolecular force field parameters for SH^-. The OPLS-AA force field [11, 12] with point charges computed by quantum chemical calculations (MP2/6-311+G(2d,2p)) was used for SH^-. The point charges listed in this table are unscaled charges, i.e. $\chi^q_{SH^-} = 1.0$. The tabulated point charges sum up to exactly -1. As explained in the main text, in our simulations, these point charges are scaled by 0.90 or 0.75.

Atom	ϵ/k_B / [K]	σ / [Å]	q / [e^-]
S	125.69	3.55	-1.04173
H	1.0000	1.00	0.04173

Table S22: Harmonic bond stretching potential parameters for SH^-. The OPLS-AA [11, 12] force field is used for SH^-. To compute the bonding potentials, we use $U_{bond} = K(r - r_0)^2$ where K is the bond coefficient, r is the distance between two atoms, and r_0 is the equilibrium distance between two atoms.

Bond	r_0 / [Å]	K/k_B / [K Å^{-2}]
S–H	1.351103	502745.3

Table S23: Number of MDEA, HCO_3^-, $MDEAH^+$, and water molecules in CO_2-loaded 50 wt.% MDEA/water solutions at 313 K as a function of CO_2 loading in the solution. To compute the self-diffusivities of CO_2, we also have two molecules of CO_2 in the solution. In these simulations, the point charges of MDEA are scaled by 0.9, and the point charges of $MDEAH^+$ and HCO_3^- are scaled by either 0.9 or 0.75. The point charges of CO_2 and water are not scaled. The average simulation box sizes are computed at 313 K and 1 bar.

CO_2 loading / [mol_{CO_2} mol^{-1}_{MDEA}]	0.01	0.1	0.5	1.0
N_{MDEA} (molar mass = 119.163 g mol^{-1})	150	205	153	29
$N_{HCO_3^-}$ (molar mass = 61.02 g mol^{-1})	1	21	148	272
N_{MDEAH^+} (molar mass = 120.17 g mol^{-1})	1	21	148	272
N_{H_2O} (molar mass = 18.02 g mol^{-1})	1000	1500	2000	2000
Average box size / [Å]	38.5	44.3	49.8	50.9

Table S24: Number of MDEA, SH^-, $MDEAH^+$, and water molecules in H_2S-loaded 50 wt.% MDEA/water solutions at 313 K as a function of H_2S loading in the solution. In these simulations, the point charges of MDEA are scaled by 0.9, and the point charges of $MDEAH^+$ and SH^- are scaled by either 0.9 or 0.75. To compute the self-diffusivities of H_2S, we also have two molecules of H_2S in the solution. The point charges of H_2S and water are not scaled. The average simulation box sizes are computed at 313 K and 1 bar.

H_2S loading / $[\mathrm{mol}_{H_2S}\ \mathrm{mol}^{-1}_{MDEA}]$	0.01	0.1	0.5	1.0
N_{MDEA} (molar mass = $119.163\,\mathrm{g\,mol^{-1}}$)	224	203	156	48
N_{SH^-}(molar mass = $33.07\,\mathrm{g\,mol^{-1}}$)	2	23	146	254
N_{MDEAH^+} (molar mass = $120.17\,\mathrm{g\,mol^{-1}}$)	2	23	146	254
N_{H_2O} (molar mass = $18.02\,\mathrm{g\,mol^{-1}}$)	1500	1500	2000	2000
Average box size / [Å]	44.0	44.2	49.3	49.9

Table S25: Speedy-Angell power equation [5] ($D_{self} = D_0 \left(\frac{T}{T_s} - 1\right)^m$) fit parameters ($D_0$, T_S and m) and coefficient of determinations (R^2) for the self diffusivity of CO_2 D_{CO_2} in aqueous MDEA solutions for different MDEA concentrations. The values of D_{CO_2} were fitted for a temperature range of 288–323 K.

MDEA concentration / [wt.%]	D_0 / $[\mathrm{m^2\,s^{-1}}]$	T_S / [K]	m	R^2
10	3.07×10^{-28}	0.710	7.14	0.992
20	3.36×10^{-47}	0.045	9.84	0.999
30	1.30×10^{-8}	238.659	1.82	0.979
40	5.80×10^{-46}	0.155	10.98	0.984
50	4.31×10^{-9}	205.738	2.70	0.992

Table S26: Speedy-Angell power equation [5] ($D_{self} = D_0 \left(\frac{T}{T_s} - 1\right)^m$) fit parameters ($D_0$, T_S and m) and coefficient of determinations (R^2) for the self diffusivity of H_2S D_{H_2S} in aqueous MDEA solutions for different MDEA concentrations. The values of D_{H_2S} were fitted for a temperature range of 288–323 K.

MDEA concentration / [wt.%]	D_0 / $[\mathrm{m^2\,s^{-1}}]$	T_S / [K]	m	R^2
10	7.78×10^{-9}	263.827	0.82	0.989
20	1.30×10^{-8}	252.324	1.49	0.991
30	7.27×10^{-9}	265.252	1.04	0.985
40	1.51×10^{-35}	0.537	9.32	0.989
50	4.34×10^{-9}	273.395	0.91	0.995

Table S27: Vogel-Tamann-Fulcher (VTF) equation [6] ($D_{\text{self}} = \exp\left[\frac{-\alpha}{T-\beta} - \gamma\right]$) fit parameters ($\alpha$, β, γ) and coefficient of determinations (R^2) for the self diffusivity of CO_2 D_{CO_2} in aqueous MDEA solutions for different MDEA concentrations. The values of D_{CO_2} were fitted for a temperature range of 288–323 K.

MDEA concentration / [wt.%]	α	β	γ	R^2
10	1.88×10^4	-5.92×10^2	-9.30×10^{-1}	0.992
20	9.02×10^5	-5.02×10^3	-1.49×10^2	0.999
30	3.67×10^2	1.91×10^2	1.73×10^1	0.979
40	3.01×10^8	-9.18×10^4	-3.25×10^3	0.988
50	1.14×10^3	1.01×10^2	1.57×10^1	0.992

Table S28: Vogel-Tamann-Fulcher (VTF) equation [6] ($D_{\text{self}} = \exp\left[\frac{-\alpha}{T-\beta} - \gamma\right]$) fit parameters ($\alpha$, β, γ) and coefficient of determinations (R^2) for the self diffusivity of H_2S D_{H_2S} in aqueous MDEA solutions for different MDEA concentrations. The values of D_{H_2S} were fitted for a temperature range of 288–323 K.

MDEA concentration / [wt.%]	α	β	γ	R^2
10	1.19×10^2	2.28×10^2	1.86×10^1	0.990
20	2.97×10^2	2.03×10^2	1.76×10^1	0.991
30	1.44×10^2	2.31×10^2	1.88×10^1	0.986
40	3.36×10^6	-1.02×10^4	-2.98×10^2	0.989
50	1.03×10^2	2.46×10^2	1.95×10^1	0.995

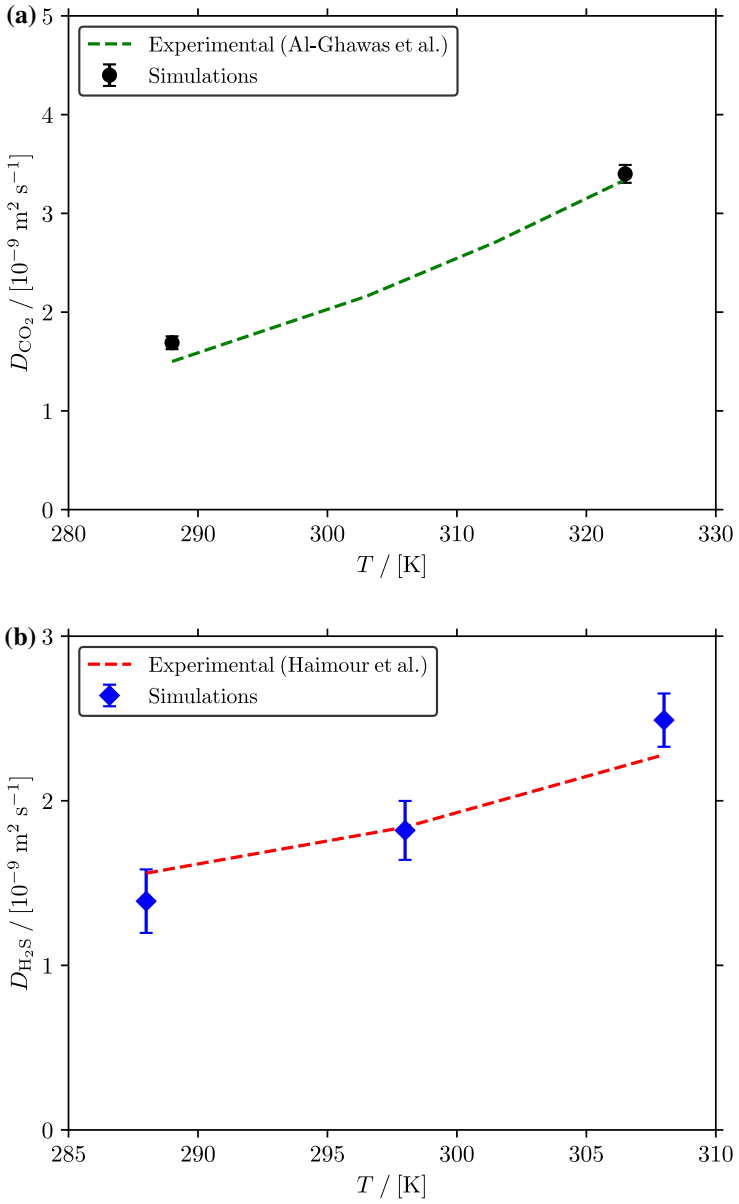

Figure S3: Computed and experimental [1, 2] self-diffusion coefficients of (a) CO_2 and (b) H_2S in pure water as a function of temperature at 1 bar. The self-diffusivities are corrected for finite-size effects using Eq. 1 of the main text. For CO_2 and H_2S, TraPPE [7, 8] force field is used while the TIP4P/2005 [9] force field is used for water (see Tables S1–S7).

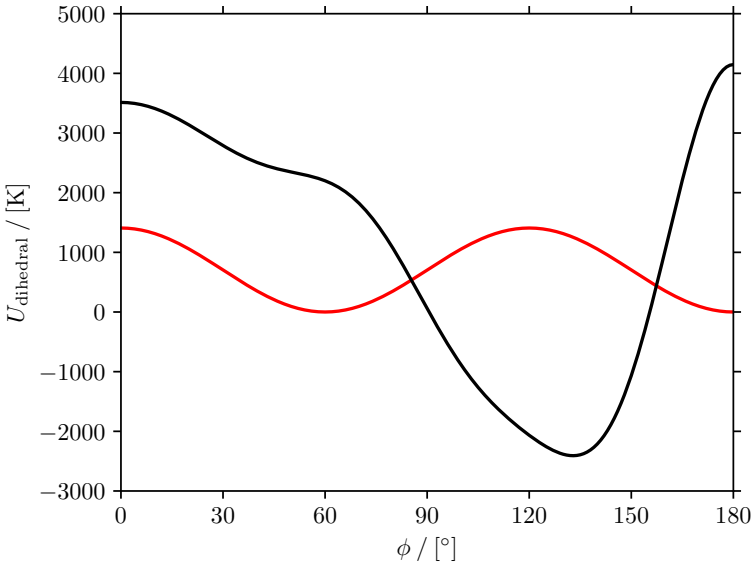

Figure S4: Dihedral potential energy as a function of dihedral angle for N–C–C–O dihedral in MDEA. The red curve represent the dihedral potential from Cornell et al. [3] (Table S11) while the black curve represent the dihedral potential from Orozco et al. [4] (Table S12).

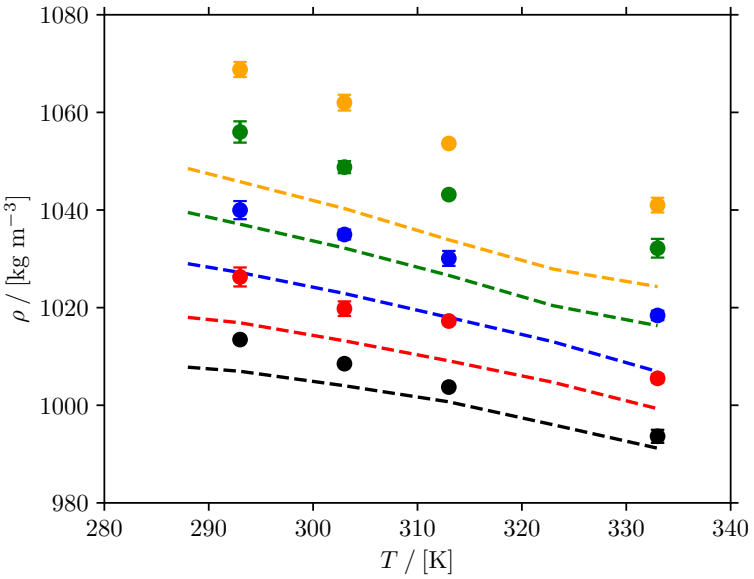

Figure S5: Computed and experimental [1] densities of aqueous MDEA solutions as a function of temperature at 1 bar. Note that the point charges of MDEA are not scaled, i.e. $\chi^q_{\mathrm{MDEA}} = 1$ and the parameters from Cornell et al. [3] are used for the N–C–C–O dihedral in MDEA. Dashed lines represent experimental results from Al-Ghawas et al. [1]. Color code: black: 10 wt.% MDEA/water; red: 20 wt.% MDEA/water; blue: 30 wt.% MDEA/water; green: 40 wt.% MDEA/water; orange: 50 wt.% MDEA/water.

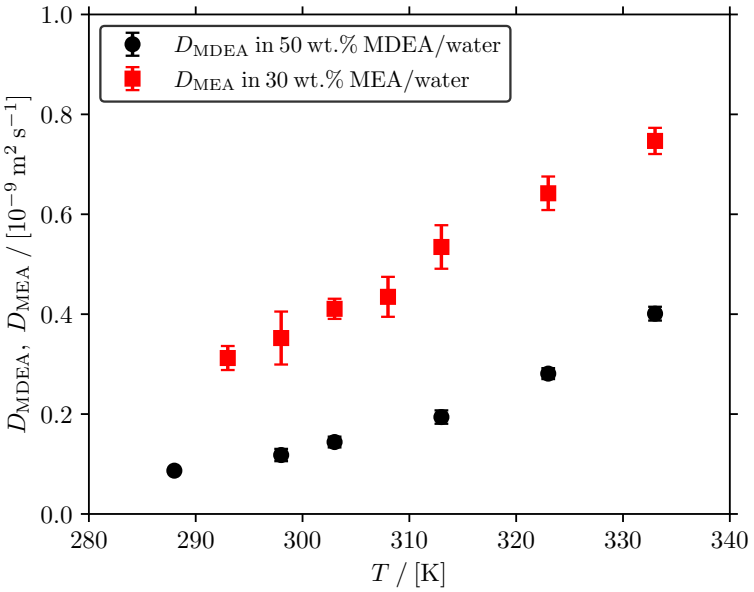

Figure S6: Comparison between the computed self-diffusities of MDEA D_{MDEA} in 50 wt% MDEA/water solution and D_{MEA} in 30 wt.% MEA/water solution [13] as a function of temperature at 1 bar. The self-diffusivities are corrected for finite-size effects using Eq. 1 of the main text. The point charges of MDEA and MEA [13] are scaled by 0.9 and 0.8, respectively. We compare the values of D_{MDEA} in a 50 wt% MDEA/water solution and the values of D_{MEA} in a 30 wt.% MEA/water solution because MDEA and MEA have similar mole fractions in these solutions ($X_{\mathrm{MDEA}} = 0.13$ in 50 wt.% MDEA/water solutions and $X_{\mathrm{MEA}} = 0.11$ in 30 wt.% MEA/water solutions).

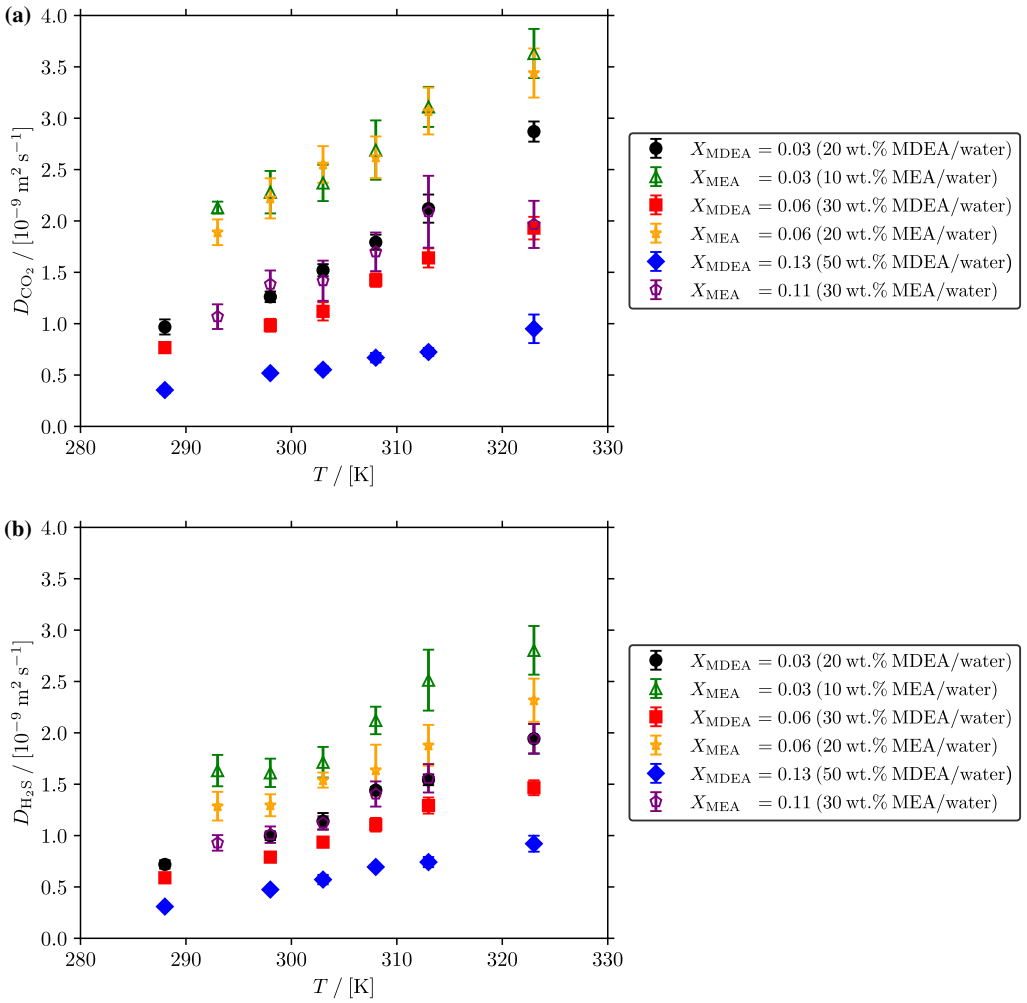

Figure S7: Comparison of (a) the self-diffusities of CO_2 D_{CO_2} and (b) the self-diffusities of H_2S D_{H_2S} in aqueous MDEA (this study) and MEA [13] solutions as a function of temperature at 1 bar. The self-diffusivities are corrected for finite-size effects using Eq. 1 of the main text. The point charges of MDEA and MEA [13] are scaled by 0.9 and 0.8, respectively. Note that due to the difference in the molar weights of MDEA and MEA, different weight percentages of MDEA and MEA can correspond to a similar molar fraction. For example, $X_{MDEA} = 0.03$ in 20 wt.% MDEA/water solutions while $X_{MEA} = 0.03$ in 10 wt.% MDEA/water solutions.

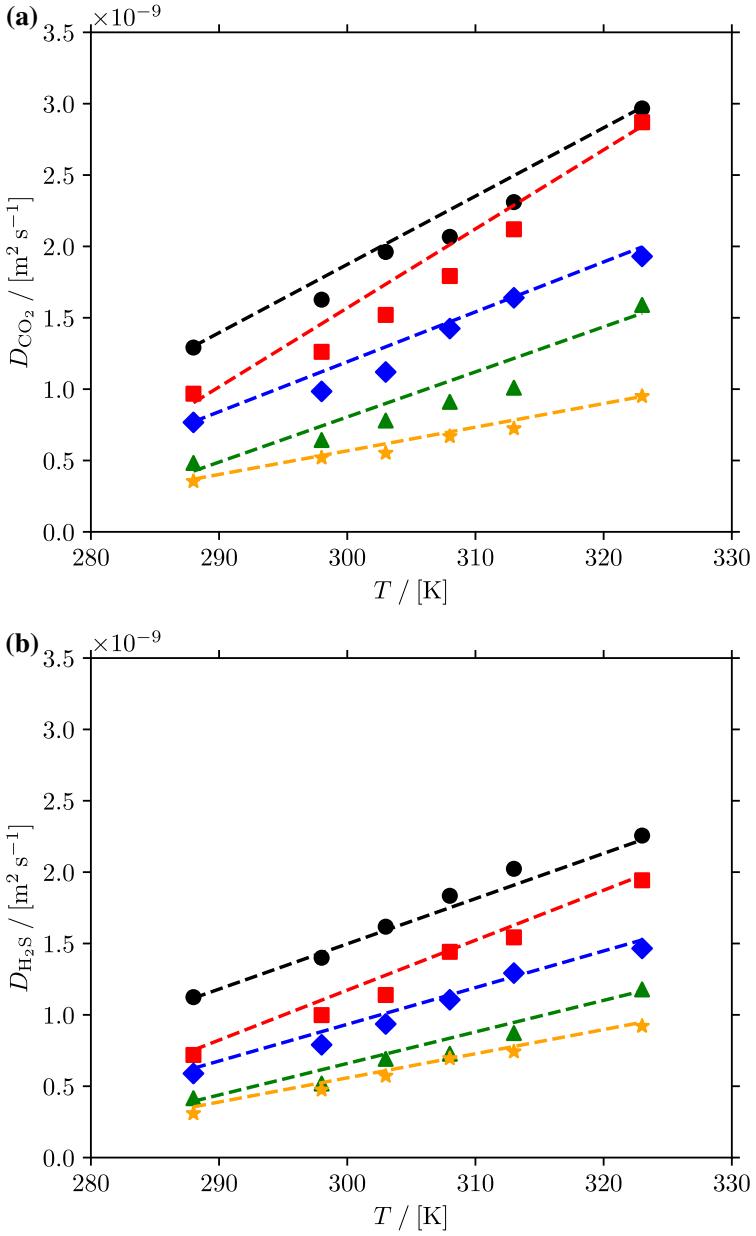

Figure S8: Computed values of (a) the self-diffusities of CO_2 D_{CO_2} and (b) the self-diffusities of H_2S D_{H_2S} as a function of temperature and MDEA concentration in the solution at 1 bar. The self-diffusivities are corrected for finite-size effects using Eq. 1 of the main text. The point charges of MDEA are scaled by 0.9. The dashed lines represent the fits to the Arrhenius equation. The color code follows that of Fig. S5.

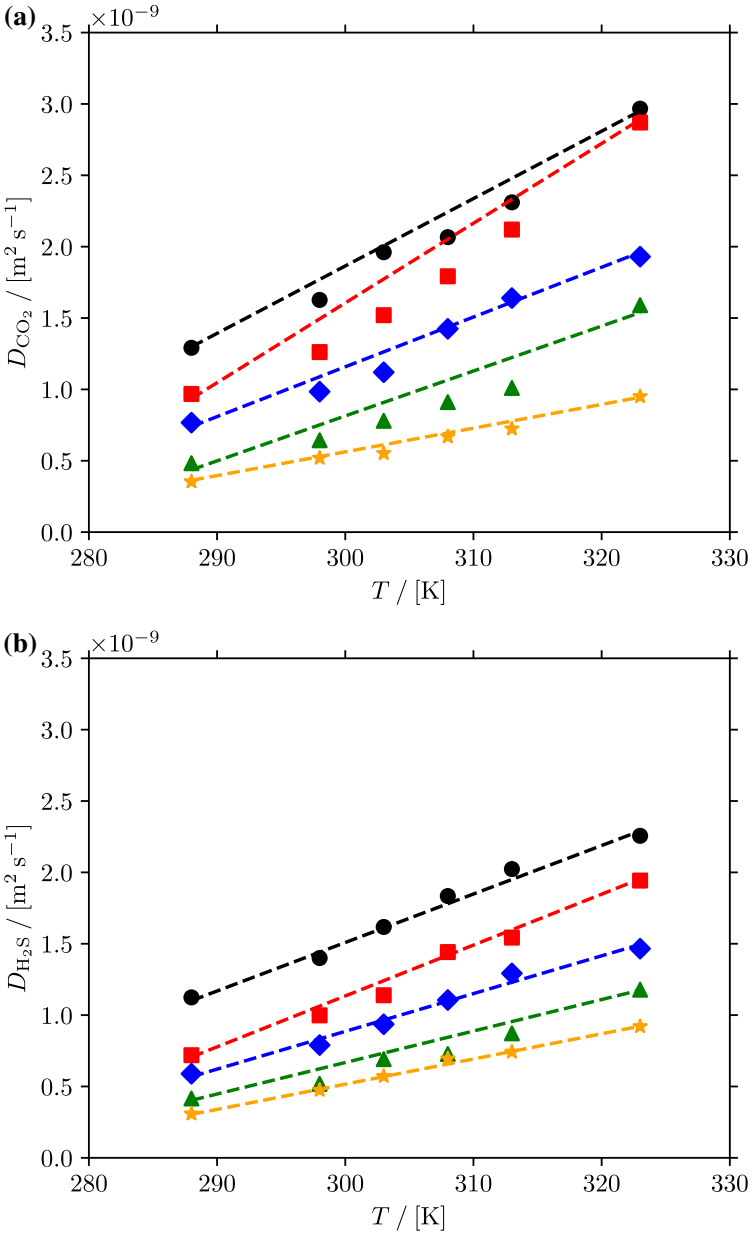

Figure S9: Computed values of (a) the self-diffusities of CO_2 D_{CO_2} and (b) the self-diffusities of H_2S D_{H_2S} as a function of temperature and MDEA concentration in the solution at 1 bar. The self-diffusivities are corrected for finite-size effects using Eq. 1 of the main text. The point charges of MDEA and MEA [13] are scaled by 0.9 and 0.8, respectively. The dashed lines represent the fits to the Speedy-Angell power equation [5]. The color code follows that of Fig. S5.

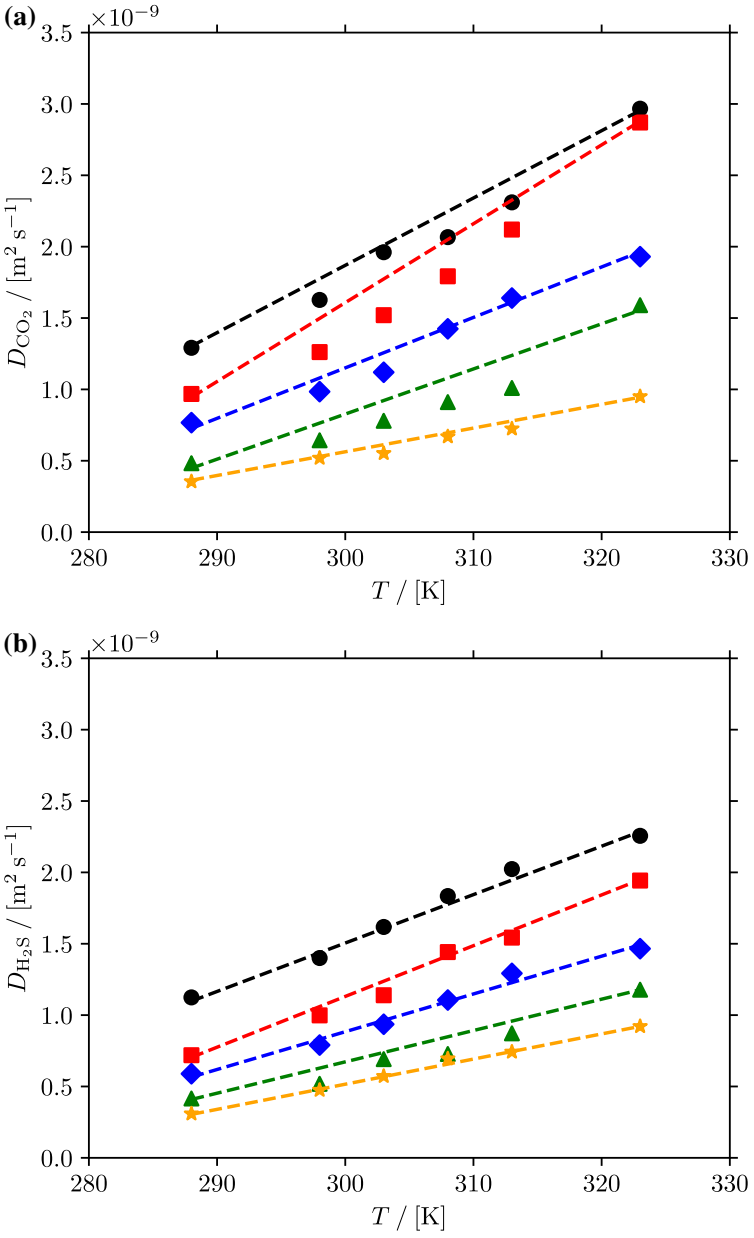

Figure S10: Computed values of (a) the self-diffusities of CO_2 D_{CO_2} and (b) the self-diffusities of H_2S D_{H_2S} as a function of temperature and MDEA concentration in the solution at 1 bar. The self-diffusivities are corrected for finite-size effects using Eq. 1 of the main text. The point charges of MDEA and MEA [13] are scaled by 0.9 and 0.8, respectively. The dashed lines represent the fits to the VTF equation [6]. The color code follows that of Fig. S5.

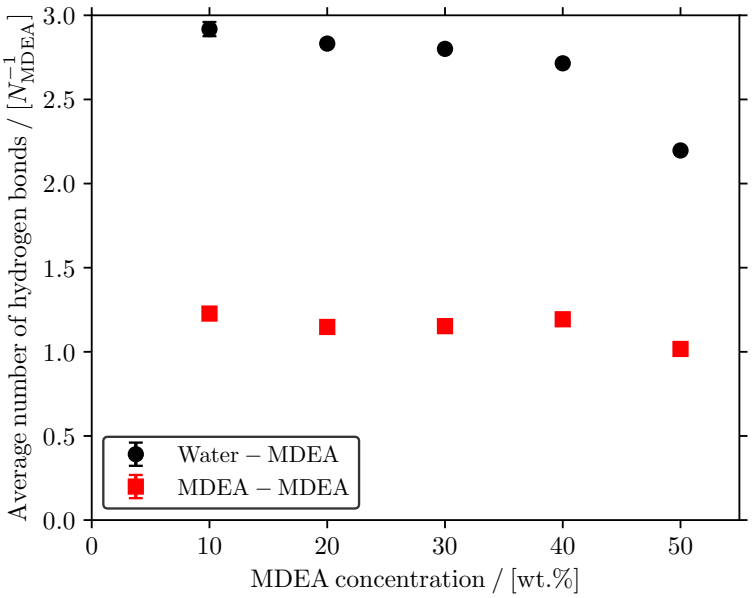

Figure S11: Average number of hydrogen bonds per MDEA molecule between water-MDEA and MDEA-MDEA pairs as a function of MDEA concentration in the solution at 313 K and 1 bar. Average number of hydrogen bonds are computed using VMD Hydrogen Bonds plugin [14] with a cutoff distance of 3.5 Å and a cutoff angle of 30° [15]. 2000 simulation snapshots are used to compute average number of hydrogen bonds.

References

[1] H. A. Al-Ghawas, D. P. Hagewiesche, G. Ruiz-Ibanez, O. C. Sandall, Physicochemical properties important for carbon dioxide absorption in aqueous methyldiethanolamine, Journal of Chemical and Engineering Data 34 (1989) 385–391.

[2] N. Haimour, O. C. Sandall, Molecular diffusivity of hydrogen sulfide in water, Journal of Chemical and Engineering Data 29 (1984) 20–22.

[3] W. D. Cornell, P. Cieplak, C. I. Bayly, I. R. Gould, K. M. Merz, D. M. Ferguson, D. C. Spellmeyer, T. Fox, J. W. Caldwell, P. A. Kollman, A second generation force field for the simulation of proteins, nucleic acids, and organic molecules, Journal of the American Chemical Society 117 (1995) 5179–5197.

[4] G. A. Orozco, V. Lachet, C. Nieto-Draghi, A. D. MacKie, A transferable force field for primary, secondary, and tertiary alkanolamines, Journal of Chemical Theory and Computation 9 (2013) 2097–2103.

[5] R. J. Speedy, C. A. Angell, Isothermal compressibility of supercooled water and evidence for a thermodynamic singularity at -45°C, The Journal of Chemical Physics 65 (1976) 851–858.

[6] W. Lu, H. Guo, I. M. Chou, R. C. Burruss, L. Li, Determination of diffusion coefficients of carbon dioxide in water between 268 and 473 K in a high-pressure capillary optical cell with in situ raman spectroscopic measurements, Geochimica et Cosmochimica Acta 115 (2013) 183–204.

[7] J. J. Potoff, J. I. Siepmann, Vapor–liquid equilibria of mixtures containing alkanes, carbon dioxide, and nitrogen, AIChE Journal 47 (2001) 1676–1682.

[8] M. S. Shah, M. Tsapatsis, J. I. Siepmann, Development of the transferable potentials for phase equilibria model for hydrogen sulfide, Journal of Physical Chemistry B 119 (2015) 7041–7052.

[9] J. L. F. Abascal, C. Vega, A general purpose model for the condensed phases of water: TIP4P/2005, Journal of Chemical Physics 123 (2005) 234505.

[10] G. A. Orozco, I. G. Economou, A. Z. Panagiotopoulos, Optimization of intermolecular potential parameters for the CO_2/H_2O mixture, Journal of Physical Chemistry B 118 (2014) 11504–11511.

[11] W. L. Jorgensen, D. S. Maxwell, J. Tirado-Rives, Development and testing of the OPLS all-atom force field on conformational energetics and properties of organic liquids, Journal of the American Chemical Society 118 (1996) 11225–11236.

[12] R. C. Rizzo, W. L. Jorgensen, OPLS all-atom model for amines: Resolution of the amine hydration problem, Journal of the American Chemical Society 121 (1999) 4827–4836.

[13] H. M. Polat, F. de Meyer, C. Houriez, C. Coquelet, O. A. Moultos, T. J. H. Vlugt, Transport properties of mixtures of acid gases with aqueous monoethanolamine solutions: A molecular dynamics study, Fluid Phase Equilibria 564 (2023) 113587.

[14] W. Humphrey, A. Dalke, K. Schulten, VMD – Visual Molecular Dynamics, Journal of Molecular Graphics 14 (1996) 33–38.

[15] A. Luzar, D. Chandler, Effect of environment on hydrogen bond dynamics in liquid water, Physical Review Letters 76 (1996) 928–931.